SMALL DISTURBANCE NAVIER-STOKES COMPUTATIONS EMPLOYING THE WILCOX K-OMEGA TURBULENCE MODEL

Alexander Pechloff [*] , **Boris Laschka** [†]
Technische Universität München, Boltzmannstr. 15, D-85748 Garching, Germany

Keywords: *small disturbance Navier-Stokes equations, computational fluid dynamics, aeroelasticity*

Abstract

Developed at Technische Universität München, the small disturbance Navier-Stokes method FLM-SD.NS has been substantiated as both an efficient and accurate means for providing unsteady air loads to the transonic aeroelastic analysis process. In an effort to extend its range of applicability, a dynamically linear instance of the Willcox k-ω eddy-viscosity closure is incorporated, complementing the original Spalart-Allmaras option. Harmonic pitching oscillations of a generic high-aspect-ratio wing are investigated. For the attached-flow cases, the k-ω incarnation of FLM-SD.NS delivers equally accurate predictions as the Spalart-Allmaras original. Reductions in computation time, up to half an order of magnitude, in relation to the comparative time-domain Reynolds-averaged Navier-Stokes method FLM-NS are again observed. For the detached-flow case, the primary benefit of the Wilcox k-ω eddy-viscosity closure is witnessed in the FLM-NS-supplied time-invariant mean solution about which FLM-SD.NS computes the dynamically linear perturbation: At localities of flow detachment, the supersonic-flow-terminating shock is rendered distinctly closer to the measured physical position than for the Spalart-Allmaras instance. Limitations of the small disturbance approach, however, become apparent for both incarnations, as a substantial degree of nonlinear interaction physically exists.

[*] Dipl.-Ing. (Univ.), Research Engineer

[†] Prof. em. Dr.-Ing.

Nomenclature

A	=	semispan planform area, $\int_0^s c\,dy$
AR	=	semispan aspect ratio, s^2/A
c	=	local chord length, $c(y/s)$
c_f	=	skin friction coefficient
c_L	=	lift coefficient, dimensional lift normalized with $\check{\rho}_\infty |\check{v}_\infty|^2 \check{A}/2$
c_M	=	moment coefficient, dimensional moment respective to the pitch axis normalized with $\check{\rho}_\infty |\check{v}_\infty|^2 \check{A}\check{c}_\mu/2$ (greater than 0: tail-heavy moment / pitch up)
c_p	=	pressure coefficient
$c_{p,crit}$	=	critical pressure coefficient, $c_p(Ma_\infty)$ at $Ma = 1.0$
c_r	=	root chord length, $c(0)$
c_t	=	tip chord length, $c(1)$
c_μ	=	reference chord length, $\int_0^s c^2\,dy/A$
D_k, D_ω	=	k-, ω-destruction term
d^+	=	sublayer-scaled distance of the first offbody grid plane
$\mathbf{E}_{v\psi}$	=	generalized viscous flux vector
$\mathbf{E}_\psi$	=	generalized convective flux vector
e	=	specific total energy
$\mathbf{F}, \mathbf{G}, \mathbf{H}$	=	convective flux vector in ξ, η, ζ direction; respectively, $\mathbf{E}_\xi$, $\mathbf{E}_\eta$, $\mathbf{E}_\zeta$

$\mathbf{F_v}, \mathbf{G_v}, \mathbf{H_v}$ = viscous flux vector in ξ, η, ζ direction; respectively, $\mathbf{E_{v\xi}}$, $\mathbf{E_{v\eta}}$, $\mathbf{E_{v\zeta}}$

f = oscillation frequency

H = total enthalpy per unit volume, $\rho e + p$

Im = imaginary part

i = imaginary unit

J = determinant of the Cartesian--to-curvilinear-coordinate transformation's Jacobian

$J\psi_x, J\psi_y, J\psi_z, J\psi_t$ = generalized metrics of the Cartesian-to-curvilinear-coordinate transformation

$\mathbf{K_\psi}$ = Jacobian matrix of $\mathbf{E_\psi}$

k = specific turbulence kinetic energy

$\check{k}$ = angular frequency, $\sqrt{\gamma} Ma_\infty k_{red}$

k_{red} = reduced oscillation frequency, $2\pi \check{f} \check{L} \sqrt{\check{\rho}_\infty} / (Ma_\infty \sqrt{\gamma \check{p}_\infty})$

L = reference length of the geometric nondimensionalization

Ma = local Mach number

Ma_∞ = freestream Mach number, $|\check{\mathbf{v}}_\infty| \sqrt{\check{\rho}_\infty} / \sqrt{\gamma \check{p}_\infty}$

P_k, P_ω = k-, ω-production term

p = static pressure

p_∞ = freestream static pressure

Pr = Prandtl number

Pr_t = turbulent Prandtl number

$\mathbf{Q}$ = conservative state vector in the $\xi\eta\zeta$ system

$\mathbf{q}$ = conservative state vector in the Cartesian coordinate system

q_x, q_y, q_z = components of the Cartesian heat-flux vector

Re = real part

Re_∞ = freestream Reynolds number, $\check{\rho}_\infty |\check{\mathbf{v}}_\infty| \check{c}_r / \check{\mu}_\infty$

S = Sutherland constant

s = semispan length

T = static temperature

T_∞ = freestream static temperature

$\mathbf{T}$ = turbulent source term vector

t = time

t_{CPU}^{method} = Institute for Fluid Mechanics method computation time

u, v, w = velocity in x, y, z direction

$|\mathbf{v}_\infty|$ = magnitude of the freestream velocity vector

x, y, z = global Cartesian coordinates

x = span-station-local chordwise coordinate, $x(y/s)$ (0: leading edge, c: trailing edge)

x_p, z_p = global pitch axis coordinates

y = semispan coordinate (0: root, s: tip)

α = incidence angle

γ = ratio of specific heats

Δ = difference between lower- and upper-surface values, $\Delta(x/c)$; for example, $\Delta c_p = c_{p,lower} - c_{p,upper}$

ζ_{CPU} = ratio of Institute for Fluid Mechanics method computation times, $\check{t}_{CPU}^{SD.NS} / \check{t}_{CPU}^{NS}$

$\check{\phi}_\chi$ = phase angle of $\hat{\chi}$, deg

λ = taper ratio, c_t / c_r

μ = molecular viscosity

μ_∞ = freestream molecular viscosity, $\mu(T_\infty)$

μ_t = eddy viscosity

ξ, η, ζ = curvilinear coordinates

Π_x, Π_y, Π_z = Cartesian energy-fluxes

ρ = density

ρ_∞ = freestream density

θ_ψ = generalized contravariant velocity multiplied by J

τ = time in the $\xi\eta\zeta$ system, t

τ_s = characteristic time, $\check{t} Ma_\infty \sqrt{\gamma \check{p}_\infty} / (\check{L} \sqrt{\check{\rho}_\infty})$

$\tau_{xx}, \tau_{yy}, \tau_{zz}$ = diagonal components of the Cartesian shear-stress tensor

$\tau_{xy}, \tau_{xz}, \tau_{yx}, \tau_{yz}, \tau_{zx}, \tau_{zy}$ = off-diagonal components of the Cartesian shear-stress tensor

$\tau_{kx}, \tau_{ky}, \tau_{kz}, \tau_{\omega x}, \tau_{\omega y}, \tau_{\omega z}$ = shear-stress equivalent k-, ω-terms

τ° = pseudo-time

Φ = instantaneous arbitrary flow quantity

χ	=	generalized load coefficient, $\chi \in \{c_p, c_L, c_M\}$
$\lvert\hat{\chi}\rvert$	=	magnitude of $\hat{\chi}$, $\sqrt{(Re\,\hat{\chi})^2 + (Im\,\hat{\chi})^2}$
ψ	=	generalized curvilinear coordinate, $\psi \in \{\xi, \eta, \zeta\}$
ω	=	specific dissipation rate

Subscripts

l	=	laminar
t	=	turbulent

Superscripts

0	=	zeroth harmonic
1	=	first harmonic
$\bar{}$	=	time-invariant mean
$\tilde{}$	=	periodic perturbation
$*$	=	linearized with respect to the perturbation
$\hat{}$	=	perturbation amplitude
$\check{}$	=	dimensional
(1)	=	homogenous in the amplitude flow quantities
(2)	=	homogenous in the amplitude metrics

1 Introduction

Production analysis of an aircraft's dynamic aeroelastic behavior in the transonic speed range requires a computational fluid dynamics (CFD) method which can supply the unsteady aerodynamic loading efficiently as well as accurately with respect to the effects of compressibility and viscosity [10]. Developed at the former Aerodynamics Division of the Institute for Fluid Mechanics (FLM)‡, Technische Universität München over the past decade, the small disturbance Navier-Stokes method FLM-SD.NS can satisfy this need [7]. Also referred to as a frequency-domain time-linearized Navier-Stokes method, it solves a system of statistically treated linear partial differential equations exclusively governing the complex amplitude of a harmonic

‡reconstituted as the Institute of Aerodynamics in 12/04

perturbation about a time-invariant mean flowfield state in pseudotime. The necessary computational effort becomes comparable to the one involved with the steady-state solution of the Reynolds-averaged Navier-Stokes (RANS) equations, yet now for an unsteady problem. This approach postulates that a considered body's minor harmonic deflections about a reference position induce a predominantly dynamically linear organized unsteadiness in the flowfield's instantaneous response: Higher-order harmonics become negligible to the point where a generally phase-shifted first harmonic prevails – a valid assumption for most problems of dynamic stability.

Next to the reference (time-invariant mean) flowfield, the small disturbance Navier-Stokes solution develops contingent on an a priori known k_{red} and amplitude surface deflection of the considered body's harmonic motion. The latter is numerically supplied by way of two computational grids. One embeds the considered body at its reference position, while the other does so at its deflected extremum position. A steady-state RANS solution realized in the reference grid for the specific Ma_∞, Re_∞, and $\check{\alpha}$ serves as the time-invariant mean flowfield. The directly obtained complex amplitude load represents the first-harmonic load, while the afore computed time-invariant mean load embodies the zeroth harmonic load.

Pertinent to the otherwise commonly employed time-domain RANS methods, the computational expense of a time-accurate solution process and the accompanied incremental grid deformation, as well as the further reduction in turnaround time and throughput due to post-processing Fourier-analysis are no longer an issue with FLM-SD.NS. The accustomed fidelity of this dynamically fully nonlinear approach, however, is retained to a high degree. FLM-SD.NS application readiness has been substantiated through investigations on harmonic oscillations of both low- and high-aspect-ratio wings, as well as a rectangular wing/nacelle configuration [8, 3]. Reductions in computation time up to an order of magnitude, in relation to the in-house time-domain RANS method FLM-NS

have been demonstrated. A concurrently developed small disturbance Navier-Stokes incarnation of the French Aerospace Research Laboratory's elsA multipurpose CFD method [5] exhibits similar advantages over its dynamically fully nonlinear counterpart.

To date, a small disturbance accordant formulation of the Spalart-Allmaras (S/A) one-equation turbulence model [11] has been employed in FLM-SD.NS by default to provide the fully-accounted $\hat{\mu}_t$. This choice has served well in accurately rendering attached unsteady boundary layers of high-Reynolds-number transonic flow and their shock interaction, while also allowing oscillating regions of very localized separation to be treated. Nevertheless, the S/A turbulence model merely encompasses a single transport equation for a μ_t-related working variable, with algebraic auxiliary functions providing the remaining closure. Consequently, certain restrictions on the flowfield's possible development are given. For cases where the degree of unsteadiness, flow separation, and involved length scales may not be a priori assessable, employing a model that better represents the physics of turbulence would be favorable. In this regard, the Wilcox k-ω turbulence model [12] as well as its later derivatives [6, 9] have seen widespread use for both steady and unsteady RANS computations, for example, becoming the standard turbulence model in the DLR-developed FLOWer [4].

In its original incarnation, the Wilcox k-ω turbulence model features two locally coupled partial differential equations – one governing k and one governing ω, with $\mu_t = \rho k / \omega$ – sans any algebraic auxiliary functions. They are referred to as the k-ω transport equation system. No wall distances need to be supplied, which for complex configurations becomes computationally expensive otherwise, as known from the S/A turbulence model's utilization. Thus, the Wilcox k-ω turbulence model lends itself even more so to a small disturbance formulation from the outset. Still, only a single such instance appears to have come to fruition over the years, although in the field of turbomachinery: Holmes et al. employ it in their principle small disturbance Navier-Stokes

computations of compressor cascade's flutter and forced response [2]. Their investigations, however, were limited to the subsonic speed range with thin attached boundary layers, while a wall function had been instated to bridge the near-wall and logarithmic region. For the particular cases, the need to fully account for $\hat{\mu}_t$ towards the lower end of the frequency spectrum is identified, whereas it suffices to merely consider $\bar{\mu}_t$ towards the higher one – the so-called frozen eddy-viscosity approach. Evidently, the latter is exclusively favored in elsA's small disturbance Navier-Stokes incarnation, as witnessed for both the initially employed S/A turbulence model [5] and the recently utilized shear-stress-transport k-ω-derivative [1].

As pertaining to the external flow problem, the three-dimensional small disturbance Navier-Stokes equations incorporating a dynamically linear formulation of the original Wilcox k-ω turbulence model are subsequently presented. The resultant FLM-SD.NS extension considers the full integration of the transport equations towards the wall boundary.

2 Theory

The k-ω transport equation system is considered to be initially formulated in nondimensionalized strong-conservation flux-vector form with respect to phase-averaged flow quantities for a body-fitted $\xi \eta \zeta$ system, while accounting for grid deformation. Individual decomposition of J, $J\psi_x$, $J\psi_y$, $J\psi_z$, $J\psi_t$, and the phase-averaged field quantities into periodically perturbed and time-invariant mean instances then renders a transport equation system in which higher-order perturbation terms abound. Deeming them negligible under the small disturbance premise, the subsequently modified transport equation system can be separated into two entities. They represent the Wilcox k-ω turbulence model's dynamically-linear perturbed and time-invariant mean state, that is, throughout the former, terms are either linear combinations of the perturbed flow quantities with time-invariant mean flow quantities or $\bar{J}$, $\overline{J\psi_x}$, $\overline{J\psi_y}$, $\overline{J\psi_z}$, or linear combinations of $\tilde{J}^*$,

$\widetilde{J\psi_x}^*$, $\widetilde{J\psi_y}^*$, $\widetilde{J\psi_z}^*$, $\widetilde{J\psi_t}^*$ with the time-invariant mean flow quantities. Restriction of the considered body to harmonic motions then allows the substitutions

$$\tilde{J}^* := \hat{J}^* e^{i\check{k}\tau},$$
$$\widehat{J\psi_x} := \widehat{J\psi_x}^* e^{i\check{k}\tau}, \quad \widehat{J\psi_y} := \widehat{J\psi_y}^* e^{i\check{k}\tau}, \quad (1)$$
$$\widehat{J\psi_z} := \widehat{J\psi_z}^* e^{i\check{k}\tau}, \quad \widehat{J\psi_t} := \widehat{J\psi_t}^* e^{i\check{k}\tau},$$

as well as

$$\tilde{\Phi}(\xi,\eta,\zeta,\tau) := \hat{\Phi}(\xi,\eta,\zeta)\, e^{i\check{k}\tau}, \quad (2)$$

wherein $\hat{\Phi} \in \mathbb{C}$. As $e^{i\check{k}\tau}$ again appears linearily in all terms of this particular equation system, it can be eliminated completely, and with it time-dependency. Ultimately, a transport equation system governing both $\hat{k}$ and $\hat{\omega}$ – and thus also $\hat{\mu}_t$ – is obtained, with respect to the unknown amplitudes of the other perturbed flow quantities. Its time-invariant mean counterpart, that is, the transport equation system governing $\bar{k}$ and $\bar{\omega}$ – and thus also $\bar{\mu}_t$ – is simply equal to the steady-state formulation of the Wilcox k-ω tubulence model for the reference grid. The preceding process conforms to the one originally applied to the S/A turbulence model. Described extensively in [7], an explicit derivation is not presented here. Subsequently, * will be dropped in connection with $\hat{}$ as the indicator of linearity, avoiding double notation.

The $\hat{k}$-$\hat{\omega}$ transport equation system is incorporated into the small disturbance Navier-Stokes equations as novel sixth and seventh components of the constituting vectors. Specifically,

$$\frac{\partial \hat{\mathbf{Q}}^{(1)}}{\partial \tau^\circ} + \frac{\partial(\hat{\mathbf{F}}^{(1)} - \hat{\mathbf{F}}_{\mathbf{v}}^{(1)})}{\partial \xi} + \frac{\partial(\hat{\mathbf{G}}^{(1)} - \hat{\mathbf{G}}_{\mathbf{v}}^{(1)})}{\partial \eta}$$
$$+ \frac{\partial(\hat{\mathbf{H}}^{(1)} - \hat{\mathbf{H}}_{\mathbf{v}}^{(1)})}{\partial \zeta} = \hat{\mathbf{S}}^{(1)} + \hat{\mathbf{S}}^{(2)}, \quad (3)$$

where the right hand side is given through

$$\hat{\mathbf{S}}^{(1)} = -i\check{k}\hat{\mathbf{Q}}^{(1)} + \hat{\mathbf{T}}^{(1)},$$

$$\hat{\mathbf{S}}^{(2)} = -\left[i\check{k}\hat{\mathbf{Q}}^{(2)} + \frac{\partial(\hat{\mathbf{F}}^{(2)} - \hat{\mathbf{F}}_{\mathbf{v}}^{(2)})}{\partial \xi} \right.$$
$$\left. + \frac{\partial(\hat{\mathbf{G}}^{(2)} - \hat{\mathbf{G}}_{\mathbf{v}}^{(2)})}{\partial \eta} + \frac{\partial(\hat{\mathbf{H}}^{(2)} - \hat{\mathbf{H}}_{\mathbf{v}}^{(2)})}{\partial \zeta} \right]$$
$$+ \hat{\mathbf{T}}^{(2)}. \quad (4)$$

The constituting vectors of the left hand side are

$$\hat{\mathbf{Q}}^{(1)} = \bar{J}\hat{\mathbf{q}} = \bar{J}\left(\hat{\rho}, \widehat{\rho u}, \widehat{\rho v}, \widehat{\rho w}, \widehat{\rho e}, \widehat{\rho k}, \widehat{\rho \omega} \right)^T, \quad (5)$$

$$\hat{\mathbf{E}}_\psi^{(1)} = \left.\frac{\partial \mathbf{E}_\psi}{\partial \mathbf{q}}\right|_{\bar{\mathbf{q}}} \hat{\mathbf{q}} = \bar{\mathbf{K}}_\psi \hat{\mathbf{q}}, \quad (6)$$

with

$$\bar{\mathbf{K}}_\psi = \begin{pmatrix} 0 & \overline{J\psi_x} & \overline{J\psi_y} & \overline{J\psi_z} & 0 & 0 & 0 \\ \overline{J\psi_x}\bar{\phi}-\bar{u}\bar{\theta}_\psi & \bar{\theta}_\psi+(1-\Gamma)\overline{J\psi_x}\bar{u} & \overline{J\psi_y}\bar{u}-\Gamma\overline{J\psi_x}\bar{v} & \overline{J\psi_z}\bar{u}-\Gamma\overline{J\psi_x}\bar{w} & \Gamma\overline{J\psi_x} & -\Gamma\overline{J\psi_x} & 0 \\ \overline{J\psi_y}\bar{\phi}-\bar{v}\bar{\theta}_\psi & \overline{J\psi_x}\bar{v}-\Gamma\overline{J\psi_y}\bar{u} & \bar{\theta}_\psi+(1-\Gamma)\overline{J\psi_y}\bar{v} & \overline{J\psi_z}\bar{v}-\Gamma\overline{J\psi_y}\bar{w} & \Gamma\overline{J\psi_y} & -\Gamma\overline{J\psi_y} & 0 \\ \overline{J\psi_z}\bar{\phi}-\bar{w}\bar{\theta}_\psi & \overline{J\psi_x}\bar{w}-\Gamma\overline{J\psi_z}\bar{u} & \overline{J\psi_y}\bar{w}-\Gamma\overline{J\psi_z}\bar{v} & \bar{\theta}_\psi+(1-\Gamma)\overline{J\psi_z}\bar{w} & \Gamma\overline{J\psi_z} & -\Gamma\overline{J\psi_z} & 0 \\ (\bar{\phi}-\Upsilon)\bar{\theta}_\psi & \Upsilon\overline{J\psi_x}-\Gamma\bar{\theta}_\psi\bar{u} & \Upsilon\overline{J\psi_y}-\Gamma\bar{\theta}_\psi\bar{v} & \Upsilon\overline{J\psi_z}-\Gamma\bar{\theta}_\psi\bar{w} & \gamma\bar{\theta}_\psi & -\Gamma\bar{\theta}_\psi & 0 \\ -\bar{k}\bar{\theta}_\psi & \overline{J\psi_x}\bar{k} & \overline{J\psi_y}\bar{k} & \overline{J\psi_z}\bar{k} & 0 & \bar{\theta}_\psi & 0 \\ -\bar{\omega}\bar{\theta}_\psi & \overline{J\psi_x}\bar{\omega} & \overline{J\psi_y}\bar{\omega} & \overline{J\psi_z}\bar{\omega} & 0 & 0 & \bar{\theta}_\psi \end{pmatrix},$$

$$\bar{\theta}_\psi = \overline{J\psi_x}\,\bar{u}+\overline{J\psi_y}\,\bar{v}+\overline{J\psi_z}\,\bar{w}, \quad \Gamma = \gamma-1, \quad \Upsilon = \gamma\bar{e}-\bar{\phi}-\Gamma\bar{k}, \quad \bar{\phi} = \Gamma(\bar{u}^2+\bar{v}^2+\bar{w}^2)/2, \quad (7)$$

as well as

$$\hat{\mathbf{E}}_{\mathbf{v}\psi}^{(1)} = \begin{pmatrix} 0 \\ \overline{J\psi_x}\hat{\tau}_{xx} + \overline{J\psi_y}\hat{\tau}_{yx} + \overline{J\psi_z}\hat{\tau}_{zx} \\ \overline{J\psi_x}\hat{\tau}_{xy} + \overline{J\psi_y}\hat{\tau}_{yy} + \overline{J\psi_z}\hat{\tau}_{zy} \\ \overline{J\psi_x}\hat{\tau}_{xz} + \overline{J\psi_y}\hat{\tau}_{yz} + \overline{J\psi_z}\hat{\tau}_{zz} \\ \overline{J\psi_x}\hat{\Pi}_x + \overline{J\psi_y}\hat{\Pi}_y + \overline{J\psi_z}\hat{\Pi}_z \\ \overline{J\psi_x}\hat{\tau}_{kx} + \overline{J\psi_y}\hat{\tau}_{ky} + \overline{J\psi_z}\hat{\tau}_{kz} \\ \overline{J\psi_x}\hat{\tau}_{\omega x} + \overline{J\psi_y}\hat{\tau}_{\omega y} + \overline{J\psi_z}\hat{\tau}_{\omega z} \end{pmatrix} , \quad (8)$$

and

$$\hat{\mathbf{T}}^{(1)} = \bar{J}\left(0, 0, 0, 0, 0, \hat{P}_k + \hat{D}_k, \hat{P}_\omega + \hat{D}_\omega\right)^T . \quad (9)$$

Correspondingly, the constituting vectors of $\hat{\mathbf{S}}^{(2)}$ are

$$\hat{\mathbf{Q}}^{(2)} = \hat{J}\bar{\mathbf{q}} = \hat{J}\left(\bar{\rho}, \overline{\rho u}, \overline{\rho v}, \overline{\rho w}, \overline{\rho e}, \overline{\rho k}, \overline{\rho \omega}, \right)^T , \quad (10)$$

$$\hat{\mathbf{E}}_{\psi}^{(2)} = \begin{pmatrix} \bar{\rho}\,\hat{\theta}_{\psi}^{(2)} \\ \overline{\rho u}\hat{\theta}_{\psi}^{(2)} + \widehat{J\psi_x}\bar{p} \\ \overline{\rho v}\hat{\theta}_{\psi}^{(2)} + \widehat{J\psi_y}\bar{p} \\ \overline{\rho w}\hat{\theta}_{\psi}^{(2)} + \widehat{J\psi_z}\bar{p} \\ \bar{H}\hat{\theta}_{\psi}^{(2)} - \widehat{J\psi_t}\bar{p} \\ \overline{\rho k}\hat{\theta}_{\psi}^{(2)} \\ \overline{\rho \omega}\hat{\theta}_{\psi}^{(2)} \end{pmatrix} , \quad (11)$$

$$\hat{\theta}_{\psi}^{(2)} = \widehat{J\psi_x}\bar{u} + \widehat{J\psi_y}\bar{v} + \widehat{J\psi_z}\bar{w} + \widehat{J\psi_t} ,$$

as well as,

$$\hat{\mathbf{E}}_{\mathbf{v}\psi}^{(2)} = \begin{pmatrix} 0 \\ \widehat{J\psi_x}\bar{\tau}_{xx} + \widehat{J\psi_y}\bar{\tau}_{yx} + \widehat{J\psi_z}\bar{\tau}_{zx} \\ \widehat{J\psi_x}\bar{\tau}_{xy} + \widehat{J\psi_y}\bar{\tau}_{yy} + \widehat{J\psi_z}\bar{\tau}_{zy} \\ \widehat{J\psi_x}\bar{\tau}_{xz} + \widehat{J\psi_y}\bar{\tau}_{yz} + \widehat{J\psi_z}\bar{\tau}_{zz} \\ \widehat{J\psi_x}\bar{\Pi}_x + \widehat{J\psi_y}\bar{\Pi}_y + \widehat{J\psi_z}\bar{\Pi}_z \\ \widehat{J\psi_x}\bar{\tau}_{kx} + \widehat{J\psi_y}\bar{\tau}_{ky} + \widehat{J\psi_z}\bar{\tau}_{kz} \\ \widehat{J\psi_x}\bar{\tau}_{\omega x} + \widehat{J\psi_y}\bar{\tau}_{\omega y} + \widehat{J\psi_z}\bar{\tau}_{\omega z} \end{pmatrix} , \quad (12)$$

and

$$\hat{\mathbf{T}}^{(2)} = \bar{J}\left(0, 0, 0, 0, 0, \bar{P}_k + \bar{D}_k, \bar{P}_\omega + \bar{D}_\omega\right)^T . \quad (13)$$

All relations needed to complete the preceding constituting vectors are compiled in Appendix A. Ultimately,

$$\hat{\mu}_t = \bar{\mu}_t\left(\frac{\hat{\rho}}{\bar{\rho}} + \frac{\hat{k}}{\bar{k}} - \frac{\hat{\omega}}{\bar{\omega}}\right) \quad (14)$$

and

$$\bar{\mu}_t = c_{P_k}\frac{\bar{\rho}\bar{k}}{\bar{\omega}} , \quad (15)$$

with

$$\begin{aligned} \hat{k} &= \left(\widehat{\rho k} - \hat{\rho}\bar{k}\right)/\bar{\rho}, & \bar{k} &= \overline{\rho k}/\bar{\rho}, \\ \hat{\omega} &= \left(\widehat{\rho \omega} - \hat{\rho}\bar{\omega}\right)/\bar{\rho}, & \bar{\omega} &= \overline{\rho \omega}/\bar{\rho}, \end{aligned} \quad (16)$$

are responsible for coupling the primary governing equations system (vector components one through five) with those of the $\hat{k}$-$\hat{\omega}$ transport equation system – witnessed in the amplitude and time-invariant mean shear-stress tensor.

The necesary small disturbance formulation of the Wilcox k-ω turbulence model's near- and far-field boundary-condition is straightforward and thus not provided here.

3 Numerical Method

FLM-SD.NS is a cell-centered structured finite volume method (multiblock capable) featuring a multigrid-accelerated implicit pseudotime-integration of the discretized small disturbance Navier-Stokes equations. Second-order spatial accuracy is given for smoothly stretched grids and regions of continuous flow, with the total variation diminishing condition yet satisfied at locations of discontinuity. Details on the numerical properties have been provided in [7, 8, 3]. The k-ω extension of FLM-SD.NS coexists with the original S/A instance in the underlying Fortran 90 code, allowing user access to either eddy viscosity closure in a single generated executable – selected case-dependently through an input parameter. Discerning the two incarnations, the designations FLM-SD.NS k-ω and FLM-SD.NS S/A are introduced.

In the past development of FLM-SD.NS, an effort had been made to retain numerical equivalence to the in-house RANS method FLM-NS, which is used, on the one hand, to supply the necessary time-invariant mean flowfield to FLM-SD.NS, while on the other hand, it is used to render a dynamically fully nonlinear solution of the particular unsteady case for comparative purposes. Therefore, the initial step towards implementing FLM-SD.NS k-ω, was to extend FLM-

NS with the Wilcox k-ω turbulence model as well. Corresponding to FLM-SD.NS, the discerning designations FLM-NS k-ω and FLM-NS S/A are employed henceforth.

The validity, limitation, and computational efficiency of FLM-SD.NS k-ω are analyzed in the following. As commonly utilized, the dynamic test cases for the generic high-aspect-ratio wing of Lockheed-Georgia, the Air Force Flight Dynamics Laboratory, NASA-Langley, and NLR [13] (LANNW) – featuring harmonic pitching oscillations – are best suited for evaluating aero-dynamic turbulence models under unsteady high-Reynolds-number transonic flow conditions: The considered motion is governed by

$$
\begin{aligned}
\check{\alpha}(k_{red}\,\tau_s) &= \check{\bar{\alpha}} + \check{\tilde{\alpha}}(k_{red}\,\tau_s) \quad \text{with} \\
\check{\tilde{\alpha}}(k_{red}\,\tau_s) &:= \check{\hat{\alpha}}\,\sin(k_{red}\,\tau_s)
\end{aligned}
\tag{17}
$$

about the given pitch axis, with $\check{\bar{\alpha}}$, $\check{\hat{\alpha}}$, and k_{red} set through the individual test case. The local unsteady load distribution normal to the wing's surface, embodied by $\bar{c}_p$, $\hat{c}_p$, as well as the resultant global loading, expressed by $\bar{c}_L$, $\hat{c}_L$ and $\bar{c}_M$, $\hat{c}_M$, are investigated. The latter are directly gained from the integration of the $\bar{c}_p$, $\hat{c}_p$ and $\bar{c}_f$, $\hat{c}_f$ distributions over the wing's reference position surface. If desired, time-dependent c_p, c_L, and c_M evolutions can be gained by recomposite, that is,

$$
\begin{aligned}
\chi(k_{red}\,\tau_s)|_{SD.NS} &:= \bar{\chi} + \tilde{\chi}(k_{red}\,\tau_s) \quad \text{with} \\
\tilde{\chi}(k_{red}\,\tau_s) &= Re\,\hat{\chi}\,\sin(k_{red}\,\tau_s) \\
&+ Im\,\hat{\chi}\,\cos(k_{red}\,\tau_s).
\end{aligned}
\tag{18}
$$

The phase angle of $\hat{\chi}$ is given through

$$
\begin{aligned}
\check{\varphi}_{\hat{\chi}} &= \left[\frac{\pi}{2}\frac{Im\,\hat{\chi}}{|Im\,\hat{\chi}|}\left(1 - \frac{Re\,\hat{\chi}}{|Re\,\hat{\chi}|}\right) \right. \\
&\left. + \arctan\left(\frac{Im\,\hat{\chi}}{Re\,\hat{\chi}}\right) \right] 180\deg / \pi,
\end{aligned}
\tag{19}
$$

with $\check{\varphi}_{\hat{\chi}} > 0$ indicating a $\tilde{\chi}$ that leads the excitation, and $\check{\varphi}_{\hat{\chi}} < 0$ indicating a $\tilde{\chi}$ that lags the excitation, respectively, according to $Im\,\hat{\chi} > 0$ and $Im\,\hat{\chi} < 0$.

In this context, the evaluation of the systemic energy transfer by $\tilde{c}_M$ over the course of a single period shows that for $\hat{\alpha} > 0$ the corresponding free pitching oscillation can be classified as unstable if $Im\,\hat{c}_M > 0$ or stable if $Im\,\hat{c}_M < 0$. This conforms, respectively, to a $\tilde{c}_M$ that either has an amplifying or a damping effect.

Primarily, prediction quality of FLM-SD.NS is assessed by comparing its time-invariant mean and complex amplitude result – the load coefficients' zeroth and first harmonic – to the one yielding from the Fourier-analyzed FLM-NS time series of a periodic cycle. The discrete evolution of c_L and c_M itself arises from the integration of the c_p and c_f distributions over the deflected wing's surface after each converged physical time step. For this purpose, the nomenclature of the FLM-SD.NS-computed load coefficients is brought into conformity with that common to the Fourier-analysis:

$$
\chi^0\big|_{SD.NS} := \bar{\chi}, \qquad \chi^1\big|_{SD.NS} := \hat{\chi}.
\tag{20}
$$

Comparing the results of FLM-SD.NS k-ω to FLM-NS k-ω, those of FLM-SD.NS S/A and FLM-NS S/A are additionally drawn upon to investigate the impact of the chosen turbulence model. FLM-NS renders the unsteady aero-dynamic loading with second-order accuracy in time. Experimental surface pressure data are also taken into account, as well as a steady-state FLOWer k-ω solution realized in the reference grid.

The LANNW's reference position is defined with respect to a globally used Cartesian coordinate system. The latter's origin, however, does not coincide with the wing's root leading edge (LE). The x (chordwise) direction runs positively toward the trailing edge (TE) and the y (spanwise) direction runs positively toward the starboard tip, rendering the designated reference plane for $\check{\alpha}$ [13]. The imposed motion is strictly longitudinal, that is, occurring about an axis parallel to the spanwise direction. Consequently, a semispan numerical treatment of the LANNW suffices, the starboard half being considered here.

4 LANN Wing

Devised as the wing of a generic transonic-transport, the LANNW is characterized by a 27 deg swept LE, a 17 deg swept TE, and a supercritical section of constant 12% relative thickness across the span ($x_d/c \approx 0.40$, round LE, sharp TE). The tip section exhibits an accrued twist of -5 deg respective the root section (Fig. 1). In its semi-span instance ($\check{L} := \check{s} = 1.000$ m), the planform is trapezoidal, with $s := \check{s}/\check{L} = 1.0$ and $c_r := \check{c}_r/\check{L} = 0.361$ supplementing the sweep angles in the definition. The secondary geometric properties result to $\lambda = 0.399$, $A := \check{A}/\check{L}^2 = 0.253$, AR $= 3.953$, and $c_\mu := \check{c}_\mu/\check{L} = 0.268$, while the pitch axis resides at $x_p/c_r = 0.62$ and $z_p = 0.00$. Surface pressure distributions were evaluated at six distinct span stations, all corresponding to those instrumented on the test model. Data for merely one inner- and one median-span station, respectively, $y_{s1} := y/s = 0.20$ and $y_{s4} = 0.65$ will be compared here.
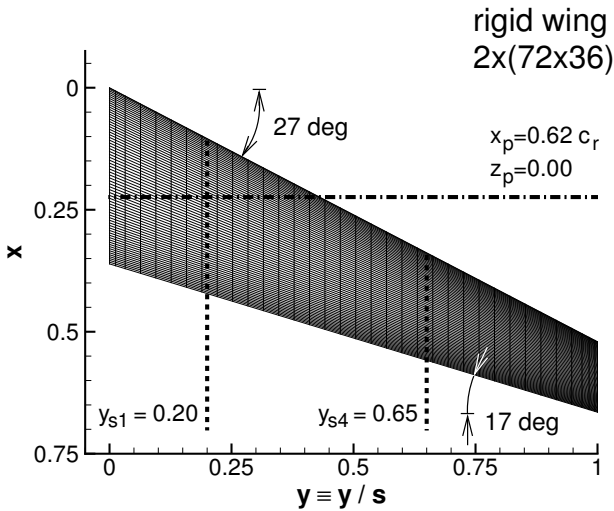
Fig. 1 LANNW semi-span surface grid with superimposed pitch axis and investigated span stations

The upper and lower surface of the LANNW's numerical embodiment are each discretized with 72 cells (hyperbolically distributed) in chordwise and 36 cells (equidistantly distributed, with segments of parabolic distribu-

tion towards root and tip) in spanwise direction, for a total of 2592 cells per surface. It is embedded (at reference position) in an elliptically smoothed two-block C-H-topology structured volume grid by way of a boundary-fitted ($\xi\eta\zeta$) coordinate system. All far-field distances are set to $3.6 \times s$ from the origin of the globally used Cartesian coordinate system, that is, in positive chordwise direction, in both positive and negative vertical (z) direction, as well as in spanwise direction respective the wing's lateral (xz) plane of symmetry. Each block discretizes approximately one half of the numerically treated physical domain. The individual block is associated with strictly one of the wing's surfaces, either the upper or lower. It discretizes the delimited volume with 96 cells in positive chordwise, 48 cells in spanwise, and 44 cells in wing surface normal direction, translating into 202,752 cells per block or 405,504 cells for the entire grid.

The grid per se has been derived from the LANNW grid employed in the FLM-SD.NS S/A investigations on high-aspect ratio wing harmonic oscillations [3] by adjusting scale and wing-surface-normal cell distribution: In regard to the former, the original grid had been constructed for $\check{L} := \check{c}_r = 0.361$ m, thus rendering the semi-span instance of the LANNW with $s := \check{s}/\check{L} = 2.77$ and $c_r := \check{c}_r/\check{L} = 1.000$. For the purpose of consistency with the NASA clipped-delta-wing grid used in [8], however, $s = 1.0$ was preferred, that is, all lengths of the original grid were divided by 2.77. In regard to the later, 40 cells had been hyperbolically distributed, with the distance of the first offbody grid plane being set to $1 \times 10^{-5} \times c_r$. For the considered high-Reynolds-number transonic flow this corresponds to a $d^+ < 5$, which had been sufficient for the S/A turbulence model, yet is not for the Wilcox k-ω one. Merely splitting each of the first two offbody cell layers in normal direction, twice in succession, however, was able to reduce the distance of the first offbody grid plane to $2.5 \times 10^{-6} \times c_r$, that is, $9 \times 10^{-7} \times s$, rendering $d^+ < 1$ as required, while retaining the original grid's four-level-multigrid capability.

The LANNW extremum grid is obtained without employing the accustomed regeneration of the volume grid and subsequent smoothing: Taking the reference grid per se, the surface grid is rotated by $\breve{\alpha}$, with all interior grid points of the block and of the *xz*-plane-of-symmetry-defining faces simply rotated in kind. Gained in this fashion, the global properties of the LANNW extremum grid naturally concur to those of the reference grid. In this context, the supplemental FLM-SD.NS/FLM-NS S/A computations employ the same reference and extremum grid as the FLM-SD.NS/FLM-NS *k*-ω ones in order to retain spatial comparability.

From the multitude of available dynamic test cases, results for a leading-edge-shock case (CT2) and a spanwise-λ-shock case (CT5), both featuring fully attached flow, as well as a spanwise-λ-shock case with partially detached flow (CT9) are presented. Table 1 provides the computation parameters for each case, with the dimensional thermodynamic reference quantities complementing $\check{L}$ provided in Table 2. All cases

Case	Ma_∞	Re_∞	$\check{\alpha}$, deg	$\breve{\alpha}$, deg	k_{red}
CT2	0.77	$7.1{\times}10^6$	0.60	0.25	0.594
CT5	0.82	$7.3{\times}10^6$	0.60	0.25	0.564
CT9	0.82	$7.2{\times}10^6$	2.60	0.25	0.560

Table 1 Computation parameters of the LANNW cases

Case	$\check{p}_\infty$, kPa	$\check{\rho}_\infty$, kg/m^3	$\check{T}_\infty$, K
CT2	100.7	1.308	268.1
CT5	95.6	1.264	263.5
CT9	95.3	1.243	267.1

Table 2 Values of the LANNW cases' dimensional thermodynamic reference quantities

have $\check{f} = 24.0$ Hz, $\gamma = 1.4$, $Pr = 0.72$ (air), and $Pr_t = 0.90$ in common. Both FLM-SD.NS *k*-ω and FLM-SD.NS S/A computations employ a three-level V-symmetric multigrid cycle for acceleration. Per multigrid cycle dual pseudotime

steps on the finest and coarsest grid level in combination with a single pseudotime step on the intermediary level (2/1/2) are conducted. A converged solution of the governing equations is assumed when the following load tolerance criterion is met, terminating the computation: At the current pseudotime step the relative change of $|\hat{c}_L|$ with respect to each $|\hat{c}_L|$ of the 30 prior pseudotime steps must be lower in absolute value than 1×10^{-5}.

For the comparative FLM-NS *k*-ω computations three oscillation cycles suffice to achieve load coefficient periodicity, each discretized with 100 physical time intervals. This is also given for the FLM-NS S/A computations of cases CT2 and CT5, with CT9, however, requiring 12 oscillation cycles, at equal temporal discretization. Incremental grid deformation is carried out through time-law accordant interpolation and extrapolation between the extremum and reference grid. Multigrid parameters and abort criterion – now naturally formulated in terms of c_L itself – are set equal to those of the FLM-SD.NS computations. All FLM-SD.NS/FLM-NS computations were conducted on a single 1.6 GHz Intel Itanium 2 processor of the Leibniz-Rechenzentrum Linux cluster. The methods' machine code was generated with the Intel Fortran Compiler for Linux. In the following, the load coefficients real and imaginary parts are normalized with $\breve{\alpha}\pi/180$ deg.

5 Results and Discussion

5.1 Leading-Edge-Shock / Attached-Flow Case

For $Ma_\infty = 0.77$, $Re_\infty = 7.1 \times 10^6$, and $\check{\alpha} = 0.60$ deg the FLM-NS supplied time-invariant mean flowfield exhibits a localized supersonic region in proximity to the upper wing surface. It extends from the root to the tip, terminating with a medium strength shock shortly downstream of the LE (Fig. 2). For the entire upper surface, flow remains attached (Fig. 3). Variations between the *k*-ω and S/A instances are marginal for both the sonic isosurface and the upper-surface isobars. FLM-SD.NS-*k*-ω-computed sur-
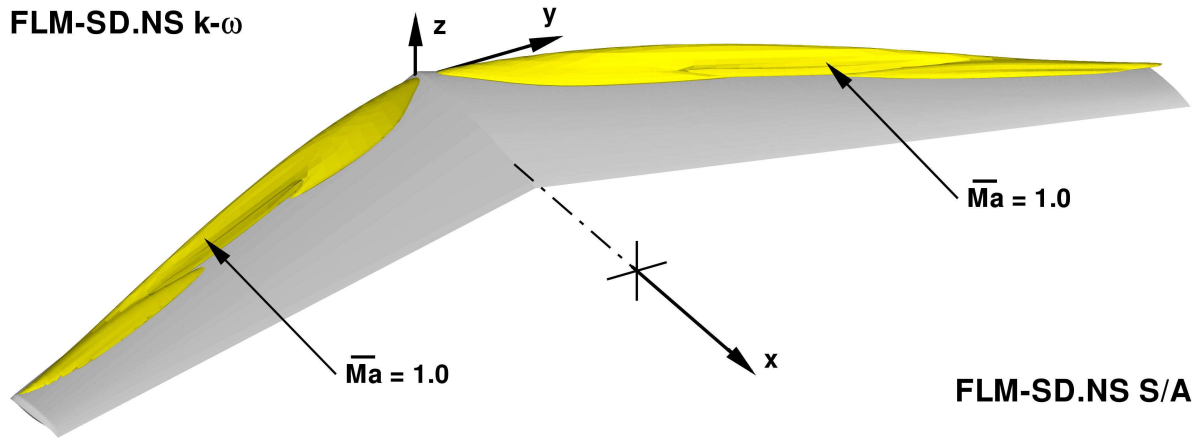
Fig. 2 Sonic isosurface of the time-invariant mean flowfields, respectively, employed by FLM-SD.NS k-ω (mirrored) and FLM-SD.NS S/A in the LANNW case CT2 ($Ma_\infty = 0.77$, $Re_\infty = 7.1 \times 10^6$, $\check{\bar{\alpha}} = 0.60$ deg, $\check{\alpha} = 0.25$ deg, $k_{red} = 0.594$, $x_p/c_r = 0.62$)
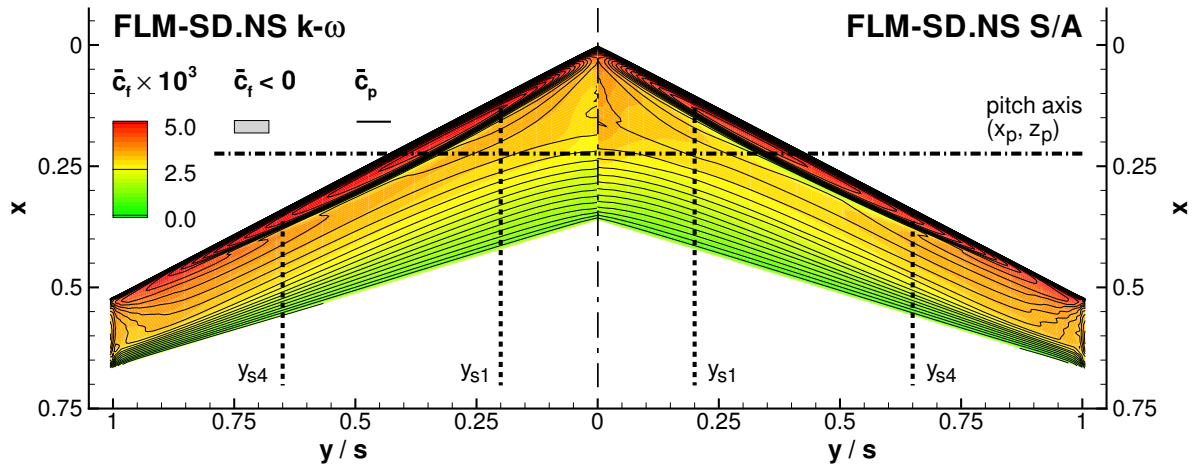

Fig. 3 Planform upper-surface skin-friction coefficient distribution (flow separation indicated by $\bar{c}_f < 0$) with superimposed isobars yielding from the time-invariant mean flowfields, respectively, employed by FLM-SD.NS k-ω (mirrored) and FLM-SD.NS S/A in the LANNW case CT2 ($Ma_\infty = 0.77$, $Re_\infty = 7.1 \times 10^6$, $\check{\bar{\alpha}} = 0.60$ deg, $\check{\alpha} = 0.25$ deg, $k_{red} = 0.594$, $x_p/c_r = 0.62$)
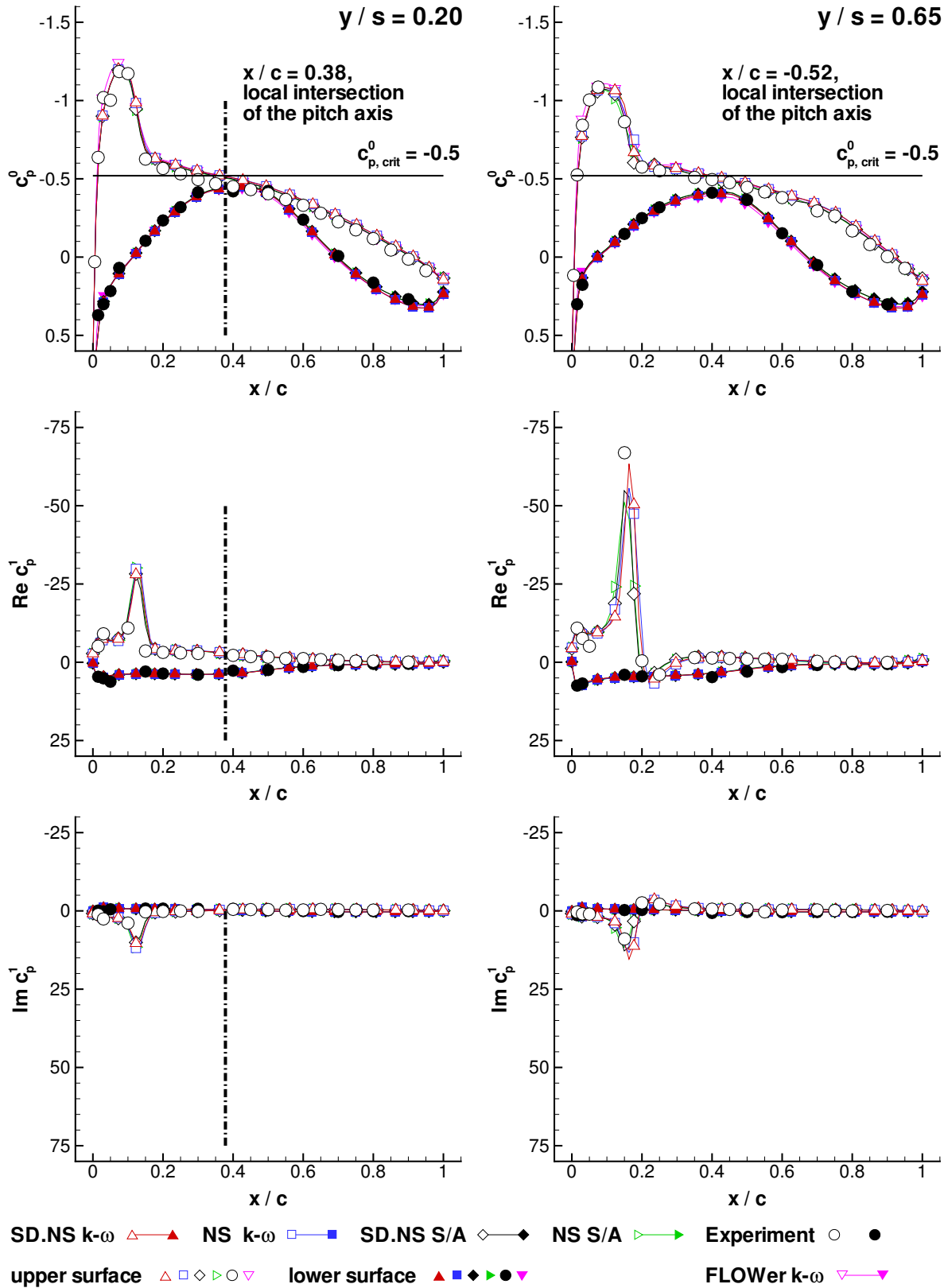
Fig. 4 Comparison of the zeroth- and first-harmonic pressure coefficient distributions (c_p^0 and c_p^1) for the LANNW case CT2 ($Ma_\infty = 0.77$, $Re_\infty = 7.1 \times 10^6$, $\check{\alpha} = 0.60$ deg, $\check{\alpha} = 0.25$ deg, $k_{red} = 0.594$, $x_p/c_r = 0.62$)

face pressure distributions for CT2 are composited with their FLM-NS k-ω, FLM-SD.NS/FLM-NS S/A, and experimental counterparts, as well as the FLOWer k-ω steady result in Fig. 4. For the investigated span stations, FLM-SD.NS-k-ω-computed c_p^0, $Re\,c_p^1$, and $Im\,c_p^1$ all agree excellently with those obtained from FLM-NS k-ω. The conformity between the two methods can be regarded equal to that between FLM-SD.NS S/A and FLM-NS S/A. Deviations in c_p^0, $Re\,c_p^1$, and $Im\,c_p^1$ between the turbulence models per se is only marginal. Experimental surface pressure is reproduced well, while FLOWer k-ω confirms the shock location.

Considering the computed global load coefficients (Table 3), both c_L^0 and $Re\,c_L^1$ gained from FLM-SD.NS k-ω agree excellently to their respective FLM-NS k-ω counterpart. FLOWer k-

FLM-method	c_L^0	$Re\,c_L^1$	$Im\,c_L^1$
SD.NS k-ω	0.353	6.071	-0.461
NS k-ω	0.355	6.079	-0.431
SD.NS S/A	0.332	5.992	-0.401
NS S/A	0.330	5.910	-0.352

FLM-method	c_M^0	$Re\,c_M^1$	$Im\,c_M^1$
SD.NS k-ω	-0.136	-1.676	-0.214
NS k-ω	-0.136	-1.604	-0.260
SD.NS S/A	-0.121	-1.652	-0.241
NS S/A	-0.121	-1.538	-0.274

Table 3 Comparison of the global load coefficients for the LANNW case CT2 ($Ma_\infty = 0.77$, $Re_\infty = 7.1 \times 10^6$, $\breve{\alpha} = 0.60$ deg, $\hat{\breve{\alpha}} = 0.25$ deg, $k_{red} = 0.594$, $x_p/c_r = 0.62$)

ω confirms either c_L^0-prediction with a value of 0.356. $Im\,c_L^1$, on the other hand, is rendered 7% higher in absolute value. This deviation, however, becomes acceptable when taking the order of magnitude into account that separates $Re\,c_L^1$ from $Im\,c_L^1$. Both computations congruently predict a time-dependent c_L that minimally lags the excitation ($\breve{\varphi}_{c_L^1} \approx -4$ deg). FLM-SD.NS-S/A-computed c_L^0 is 6% lower than its k-ω counter-

part, a difference accrued through the marginally narrower lower- and upper-surface sectional c_p^0 progression – thus yielding a smaller sectional c_L^0 – across the semispan. In contrast, FLM-SD.NS-S/A-computed $Re\,c_L^1$ can be considered identical to its k-ω counterpart, attributable to the two method's excellent conformity in the prediction of the $Re\,c_p^1$-shock-peak. For both c_L^0 and $Re\,c_L^1$ the deviation of the S/A methods is just as negligible as that of the k-ω methods before. Comparably, $Im\,c_L^1$ appears to be more susceptible to the choice of turbulence model, as well as the method type per se: FLM-SD.NS-S/A-computed $Im\,c_L^1$ is 13% lower in absolute value than its k-ω counterpart. Evidently, the reduced order of the $Im\,c_p^1$ progression, in conjunction with the significantly subdued shock peak, allows minor variations in the two methods' prediction to become amplified towards $Im\,c_L^1$. At 14%, the deviation between FLM-SD.NS-S/A- and FLM-NS-S/A-computed $Im\,c_L^1$ is double the one witnessed between the FLM-SD.NS-k-ω- and FLM-NS-k-ω-computed instances. Thus, it can be reciprocally argued that the latter methods would already agree better in their predicted $Im\,c_p^1$ progressions than is the case for their S/A counterparts, even if not readily apparent in the sectional comparison. Nevertheless, the mean of the FLM-SD.NS-S/A- and FLM-NS-S/A-computed $\breve{\varphi}_{c_L^1}$ can be considered to conform to its k-ω counterpart.

FLM-SD.NS-k-ω-predicted c_M^0 equals its FLM-NS k-ω counterpart, confirmed by FLOWer k-ω with a predicted value of -0.135. In contrast, $Re\,c_M^1$ and $Im\,c_M^1$ are, respectively, gained 4% higher and 18% lower in absolute value. Apparently, the particular deviation exhibited in $Re\,c_L^1$ and in $Im\,c_L^1$ has followed through to $Re\,c_M^1$ and $Im\,c_M^1$, even with amplification. $Im\,c_M^1$, however, is observed to be an order of magnitude smaller than $Re\,c_M^1$, rendering this circumstance again tolerable. For either method $Re\,c_M^1$ and $Im\,c_M^1$ conform in their negative sign (pitch down), congruently predicting a time-dependent c_M that lags the excitation by nearly half a cycle ($\breve{\varphi}_{c_M^1} \approx -172$ deg). In the case of a free pitching oscillation, c_M would consequently have a damping

effect. FLM-SD.NS-S/A-predicted c_M^0 is 11% lower in absolute value than its k-ω counterpart, with $Re\,c_M^1$ being gained nearly identical. $Im\,c_M^1$, on the other hand, is rendered 13% higher in absolute value. Just as the FLM-SD.NS- and FLM-NS-computed c_M^0 instances are again equal for the S/A turbulence model, the two methods' deviation in their $Re\,c_M^1$- as well as $Im\,c_M^1$-prediction is similar to the one observed between the k-ω incarnations: FLM-SD.NS-S/A-computed $Re\,c_M^1$ is gained 7% higher than the FLM-NS-S/A-computed instance in absolute value, while $Im\,c_M^1$ is rendered 12% lower, correspondingly. With respect to the k-ω predictions, the deviation has increased for the former yet decreased for the latter, albeit only marginally. The greater sensitivity of $Im\,c_L^1$ to the choice of turbulence model and method type has apparently followed through to $Im\,c_M^1$. Nevertheless, the mean of the FLM-SD.NS-S/A- and FLM-NS-S/A-computed $\check{\phi}_{c_M^1}$ can be considered to conform to its k-ω counterpart.

Overall, FLM-SD.NS k-ω renders the unsteady loading of the LE-shock case in very good agreement to FLM-NS k-ω. Prediction accuracy can be considered equal to that of their S/A counterparts.

5.2 Spanwise-λ-Shock / Attached-Flow Case

For $Ma_\infty = 0.82$, $Re_\infty = 7.3 \times 10^6$, and $\check{\alpha} = 0.60$ deg the FLM-NS supplied time-invariant mean flowfield exhibits an expanded supersonic region in proximity to the upper wing surface. It extends from the root to the tip, terminating with a medium strength shock substantially downstream of the LE (Fig. 5). Additionally, a weaker shock is initiated at the root LE, which eventually merges with the former at $y/s \approx 0.45$ to constitute the spanwise-λ-shock system. For the entire upper surface, flow remains attached (Fig. 6). Variations between the k-ω and S/A instances have become more notable for both the sonic isosurface and the upper-surface isobars, witnessed especially with respect to the shock that terminates supersonic flow (SSF). FLM-SD.NS-k-ω-computed surface pressure distributions for CT5

are composited with their FLM-NS k-ω, FLM-SD.NS/FLM-NS S/A, and experimental counterparts, as well as the FLOWer k-ω steady result in Fig. 7. For the investigated span stations, FLM-SD.NS-k-ω-computed c_p^0, $Re\,c_p^1$, and $Im\,c_p^1$ again all agree excellently with those obtained from FLM-NS k-ω. The conformity between the two methods can be regarded equal to that between FLM-SD.NS S/A and FLM-NS S/A. However, somewhat greater deviations in c_p^0, $Re\,c_p^1$, and $Im\,c_p^1$ between the turbulence models than witnessed for CT2 occur: FLM-SD.NS/FLM-NS S/A predict the SSF-terminating shock position slightly farther upstream, that is, $\approx 4\% c$ as exhibited by c_p^0. This circumstance naturally follows through to the associated $Re\,c_p^1$- and $Im\,c_p^1$-peak, also marginally influencing their magnitude and shape. Both the experimental surface pressure - otherwise reproduced well – and FLOWer k-ω appear to favor the FLM-SD.NS/FLM-NS S/A prediction over the k-ω one.

Focusing on the computed global coefficients (Table 4), FLM-SD.NS-k-ω-rendered c_L^0 and $Re\,c_L^1$ can be considered equal to their respective FLM-NS-k-ω-yielding counterpart. FLOWer

FLM-method	c_L^0	$Re\,c_L^1$	$Im\,c_L^1$
SD.NS k-ω	0.395	7.071	-1.619
NS k-ω	0.397	7.100	-1.644
SD.NS S/A	0.358	6.874	-1.226
NS S/A	0.357	6.811	-1.130

FLM-method	c_M^0	$Re\,c_M^1$	$Im\,c_M^1$
SD.NS k-ω	-0.152	-2.489	0.187
NS k-ω	-0.153	-2.473	0.154
SD.NS S/A	-0.128	-2.277	-0.080
NS S/A	-0.128	-2.181	-0.168

Table 4 Comparison of the global load coefficients for the LANNW case CT5 ($Ma_\infty = 0.82$, $Re_\infty = 7.3 \times 10^6$, $\check{\alpha} = 0.60$ deg, $\check{\alpha} = 0.25$ deg, $k_{red} = 0.564$, $x_p/c_r = 0.62$)

k-ω again confirms either c_L^0-prediction with a value of 0.389 – a deviation of merely 2%. With
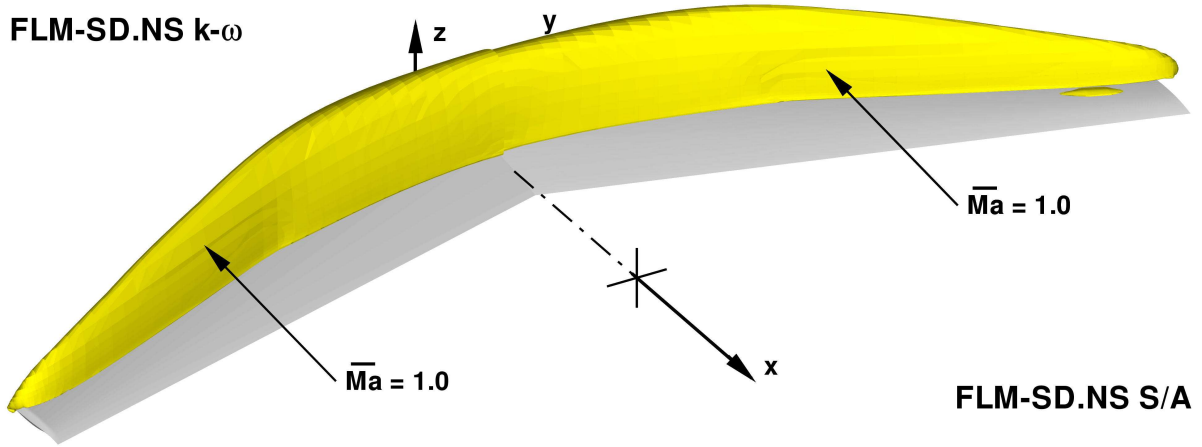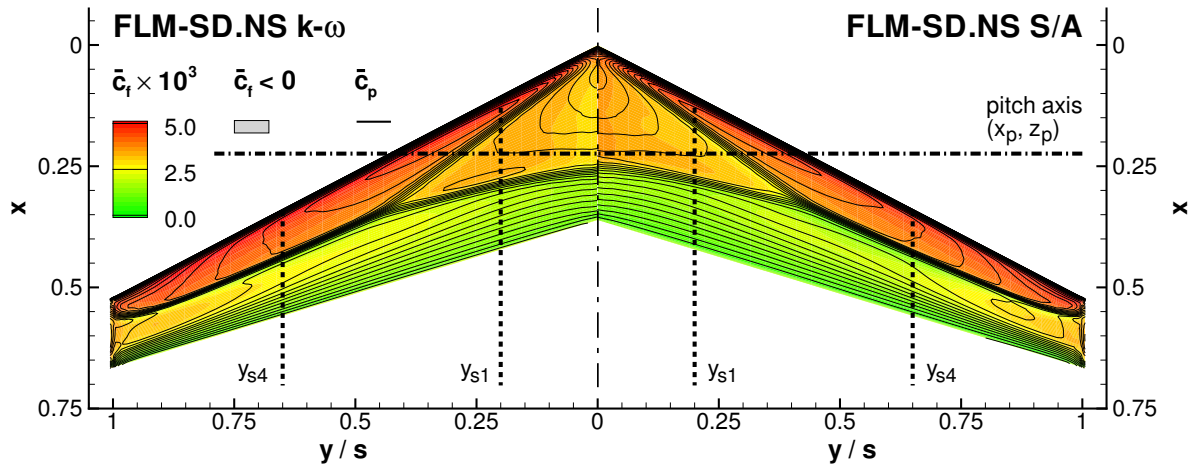
Fig. 5 Sonic isosurface of the time-invariant mean flowfields, respectively, employed by FLM-SD.NS k-ω (mirrored) and FLM-SD.NS S/A in the LANNW case CT5 ($Ma_\infty = 0.82$, $Re_\infty = 7.3 \times 10^6$, $\check{\alpha} = 0.60$ deg, $\check{\alpha} = 0.25$ deg, $k_{red} = 0.564$, $x_p/c_r = 0.62$)

Fig. 6 Planform upper-surface skin-friction coefficient distribution (flow separation indicated by $\bar{c}_f < 0$) with superimposed isobars yielding from the time-invariant mean flowfields, respectively, employed by FLM-SD.NS k-ω (mirrored) and FLM-SD.NS S/A in the LANNW case CT5 ($Ma_\infty = 0.82$, $Re_\infty = 7.3 \times 10^6$, $\check{\alpha} = 0.60$ deg, $\check{\alpha} = 0.25$ deg, $k_{red} = 0.564$, $x_p/c_r = 0.62$)

Fig. 7 Comparison of the zeroth- and first-harmonic pressure coefficient distributions (c_p^0 and c_p^1) for the LANNW case CT5 ($Ma_\infty = 0.82$, $Re_\infty = 7.3 \times 10^6$, $\breve{\alpha} = 0.60$ deg, $\breve{\alpha} = 0.25$ deg, $k_{red} = 0.564$, $x_p/c_r = 0.62$)

respect to the CT2 case, the spread between FLM-SD.NS-k-ω- and FLM-NS-k-ω-computed $Im c_L^1$ has narrowed to near congruency of the two instances. In absolute value, $Im c_L^1$ is now only half an order of magnitude smaller than $Re c_L^1$, as the prominence of the $Im c_p^1$-peak associated with the SSF-terminating shock has increased significantly across the semispan. Consequently, the time-dependent c_L lags the excitation more distinctly than before ($\check{\phi}_{c_L^1} \approx -13$ deg). FLM-SD.NS-S/A-computed c_L^0 is 9% lower than its k-ω counterpart, a difference accrued through the slightly farther upstream prediction of the SSF-terminating shock – thus yielding a smaller sectional c_L^0 – across the semispan. This circumstance puts the sensitivity of the c_L^0-prediction to the employed turbulence model even more into evidence than before: An apparent, yet only localized variation, in the upper-surface c_p^0-progression that could be considered marginal amplifies in the integration of Δc_p^0 over the entire wing to a distinct c_L^0-difference. In contrast, FLM-SD.NS-S/A-computed $Re c_L^1$ is merely 3% lower than its k-ω counterpart: Despite the inevitable difference in position, the $Re c_p^1$-peak associated with the SSF-terminating shock is rendered in good conformity with respect to magnitude and shape by the two methods. Of course, the respectively-resultant local $\Delta Re c_p^1$ contribute almost equally to the pertinent $Re c_L^1$ across the semispan. For both c_L^0 and $Re c_L^1$ the deviation of the S/A methods is just as negligible as that of the k-ω methods before. In comparison to the CT2 case, $Im c_L^1$ presents itself even more susceptible to the choice of turbulence model, yet somewhat less to the method type. FLM-SD.NS-S/A-computed $Im c_L^1$ is now 24% lower in absolute value than its k-ω counterpart, attributable to a notably reduced magnitude of the $Im c_p^1$-peak associated with the SSF-terminating shock. At 8%, a distinct deviation between FLM-SD.NS-S/A- and FLM-NS-S/A-computed $Im c_L^1$ emerges, where one had not between the FLM-SD.NS-k-ω- and FLM-NS-k-ω-computed instances. Again, it can be deduced that the latter methods must already agree better in their

predicted $Im c_p^1$ progressions than is the case for their S/A counterparts. With the mean of the FLM-SD.NS-S/A- and FLM-NS-S/A-computed $\check{\phi}_{c_L^1}$ being marginally in the negative double-digit degree range, it can still be considered to conform to its k-ω counterpart.

FLM-SD.NS-k-ω-predicted c_M^0 and $Re c_M^1$ are both nearly identical to their respective FLM-NS k-ω counterpart, FLOWer k-ω confirming c_M^0 with a computed value of -0.147 – a deviation of merely 3%. In contrast, $Im c_M^1$ is gained 21% higher, despite having observed near congruency of the corresponding $Im c_L^1$ instances. Similar to the CT2 case, $Im c_M^1$ emerges an order of magnitude smaller than $Re c_M^1$, making this circumstance again tolerable. For either method, however, $Re c_M^1$ and $Im c_M^1$ no longer conform in their sign, the positive $Im c_M^1$ (pitch up) now indicating a time-dependent c_M that leads the excitation by nearly half a cycle ($\check{\phi}_{c_M^1} \approx 176$ deg). In the case of a free pitching oscillation, c_M would consequently have an amplifying effect. FLM-SD.NS-S/A-predicted c_M^0 and $Re c_M^1$ are, respectively, gained 16% and 9% lower in absolute value than their k-ω counterparts, a behavior consistent with the SSF-terminating shock's farther upstream prediction: Across the semispan, the positive Δc_p^0 and $\Delta Re c_p^1$ of the pertinent shock region have become less leveraged towards the pitch axis, resulting in reduced sectional pitch-down contributions. FLM-SD.NS-S/A-predicted $Im c_M^1$ differs even more substantially to its k-ω counterpart. It is barely half the absolute value, while exhibiting a negative sign (pitch down): As observed before, the $Im c_p^1$-peak associated with the SSF-terminating shock has become notably subdued in its farther upstream prediction. Hence, the pertinent $\Delta Im c_p^1$ is not only leveraged lesser towards the pitch axis, but also of lesser negative value per se. Dually, the sectional pitch-up contribution to $Im c_M^1$ is mitigated across the semispan to the point where an overall pitch-down bias remains. FLM-SD.NS- and FLM-NS-computed c_M^0 instances are again equal for the S/A turbulence model, with their $Re c_M^1$-predictions deviating by a mere 4%, a marginal increase from

the near identity observed between the k-ω incarnations. For $Im c_M^1$, on the other hand, the spread has increased substantially, with the FLM-SD.NS-S/A-computed absolut value only being half of its FLM-NS-S/A counterpart. Similar to the CT2 case, the greater sensitivity of $Im c_L^1$ to the choice of turbulence model and method type has followed through to $Im c_M^1$. Since both $Im c_M^1$ are still an order of magnitude smaller than their correspondent $Re c_M^1$, this circumstance is still tolerable: Both FLM-SD.NS-S/A and FLM-NS-S/A render a time-dependent c_M that lags the excitation by nearly half a cycle (mean $\breve{\phi}_{c_M^1} \approx -177$ deg). In the case of a free pitching oscillation, c_M would consequently have a damping effect. At first glance a disparity appears to be given between the S/A- and k-ω-prediction of the stability behavior. For either turbulence model, however, the rendered time-dependent c_M may just as well be perceived as being entirely out of phase, that is, both conforming in their indication of an indifferent free pitching oscillation.

Overall, FLM-SD.NS k-ω renders the unsteady loading of the spanwise-λ-shock/attached-flow case in very good agreement to FLM-NS k-ω. Prediction accuracy with respect to that of their S/A counterparts lies within the commonly known variation between the two turbulence models.

5.3 Spanwise-λ-Shock / Detached-Flow Case

For $Ma_\infty = 0.82$, $Re_\infty = 7.2 \times 10^6$, and $\breve{\alpha} = 2.60$ deg the FLM-NS supplied time-invariant mean flowfield exhibits an even more expanded supersonic region in proximity to the upper wing surface than observed for CT5. It extends from the root to the tip, terminating with a shock that increases spanwise in strength, respectively, from medium to strong (Fig. 8). The shock initiated at the root LE now merges farther inboard with the former, while having decreased in strength. On the upper surface, flow is no longer entirely attached (Fig. 9). Variations between the k-ω and S/A instances have become very evident for both the sonic isosurface and the upper-surface isobars, due to a substantially dif-

fering flow topology. Whereas FLM-NS k-ω predicts a very localized region of flow detachment downstream of the SSF-terminating shock, the FLM-NS S/A computation yields an extensive one, that even defies reattachment towards the TE: For $y/s \approx 0.65$ the SSF-terminating shock has its farthest upstream position – within $10\%c$ of the LE. FLM-SD.NS-k-ω-computed surface pressure distributions for CT9 are composited with their FLM-NS k-ω, FLM-SD.NS/FLM-NS S/A, and experimental counterparts, as well as the FLOWer k-ω steady result in Fig. 10. For the investigated span stations, FLM-SD.NS-k-ω-computed c_p^0 again agrees excellently with the one obtained from FLM-NS k-ω. With respect to $Re c_p^1$ and $Im c_p^1$, however, substantial deviations are observed for the peaks associated with the SSF-terminating shock at the localities of flow detachment, indicating that the premise of the dynamically linear approach may no longer be valid here. It is known from the experimental data that, even for a small amplitude of $\breve{\alpha} = 0.25$ deg, the imposed motion on both the shock and the region of detached flow, as well as their dynamic interaction, are sufficient to induce significant higher-order harmonics within the time-dependent evolution of the upper-surface c_p. This can also be put into evidence by investigating the planform upper-surface second and third harmonic pressure coefficient distributions gained from FLM-NS. As discussed in [8], for regions where the higher-order harmonics are no longer negligible, the small disturbance method cannot render an accurate first harmonic prediction. Nevertheless, conformity between the two methods can be regarded similar to that between FLM-SD.NS S/A and FLM-NS S/A, however, with somewhat less deviation in the predictions of the $Re c_p^1$- and $Im c_p^1$-peak associated with the SSF-terminating shock seen for k-ω. Most importantly, however, the k-ω turbulence model per se renders the position of the SSF-terminating shock more closely to the measured physical position at localities of flow detachment than the S/A one. The FLOWer k-ω steady result supports this circumstance.

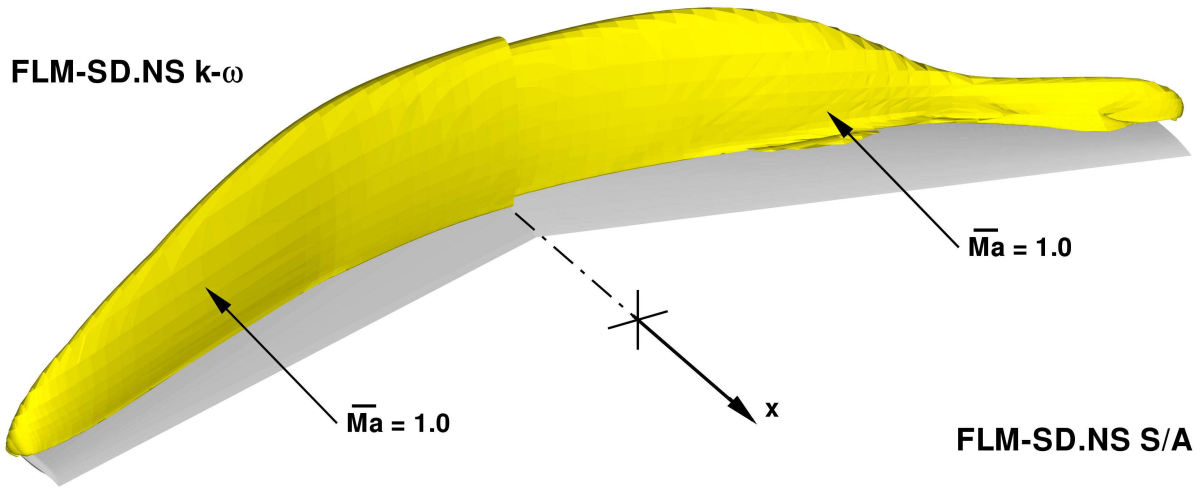Regarding the computed global load coeffi-

Fig. 8 Sonic isosurface of the time-invariant mean flowfields, respectively, employed by FLM-SD.NS k-ω (mirrored) and FLM-SD.NS S/A in the LANNW case CT9 ($Ma_\infty = 0.82$, $Re_\infty = 7.2 \times 10^6$, $\check{\alpha} = 2.60$ deg, $\check{\alpha} = 0.25$ deg, $k_{red} = 0.564$, $x_p/c_r = 0.62$)
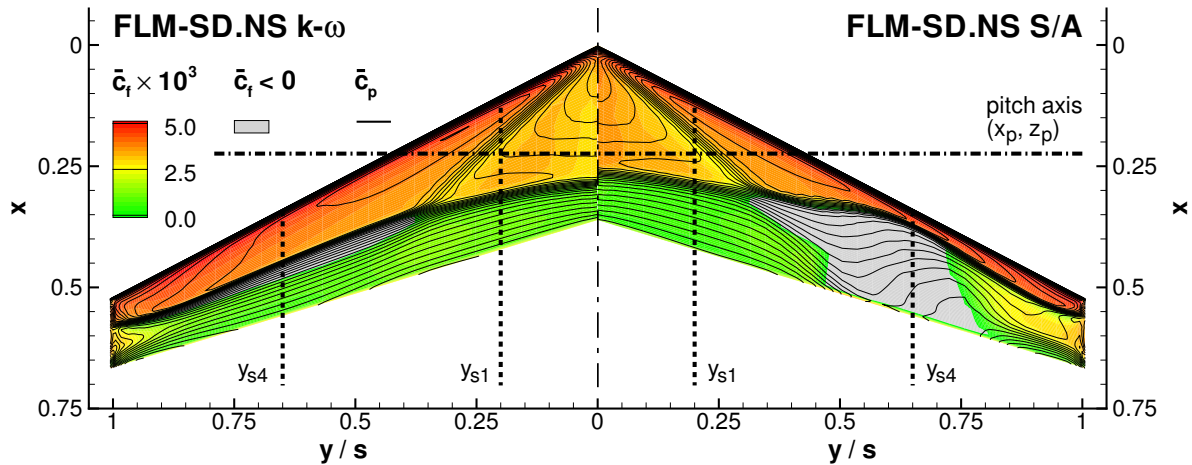

Fig. 9 Planform upper-surface skin-friction coefficient distribution (flow separation indicated by $\bar{c}_f < 0$) with superimposed isobars yielding from the time-invariant mean flowfields, respectively, employed by FLM-SD.NS k-ω (mirrored) and FLM-SD.NS S/A in the LANNW case CT9 ($Ma_\infty = 0.82$, $Re_\infty = 7.2 \times 10^6$, $\check{\alpha} = 2.60$ deg, $\check{\alpha} = 0.25$ deg, $k_{red} = 0.564$, $x_p/c_r = 0.62$)
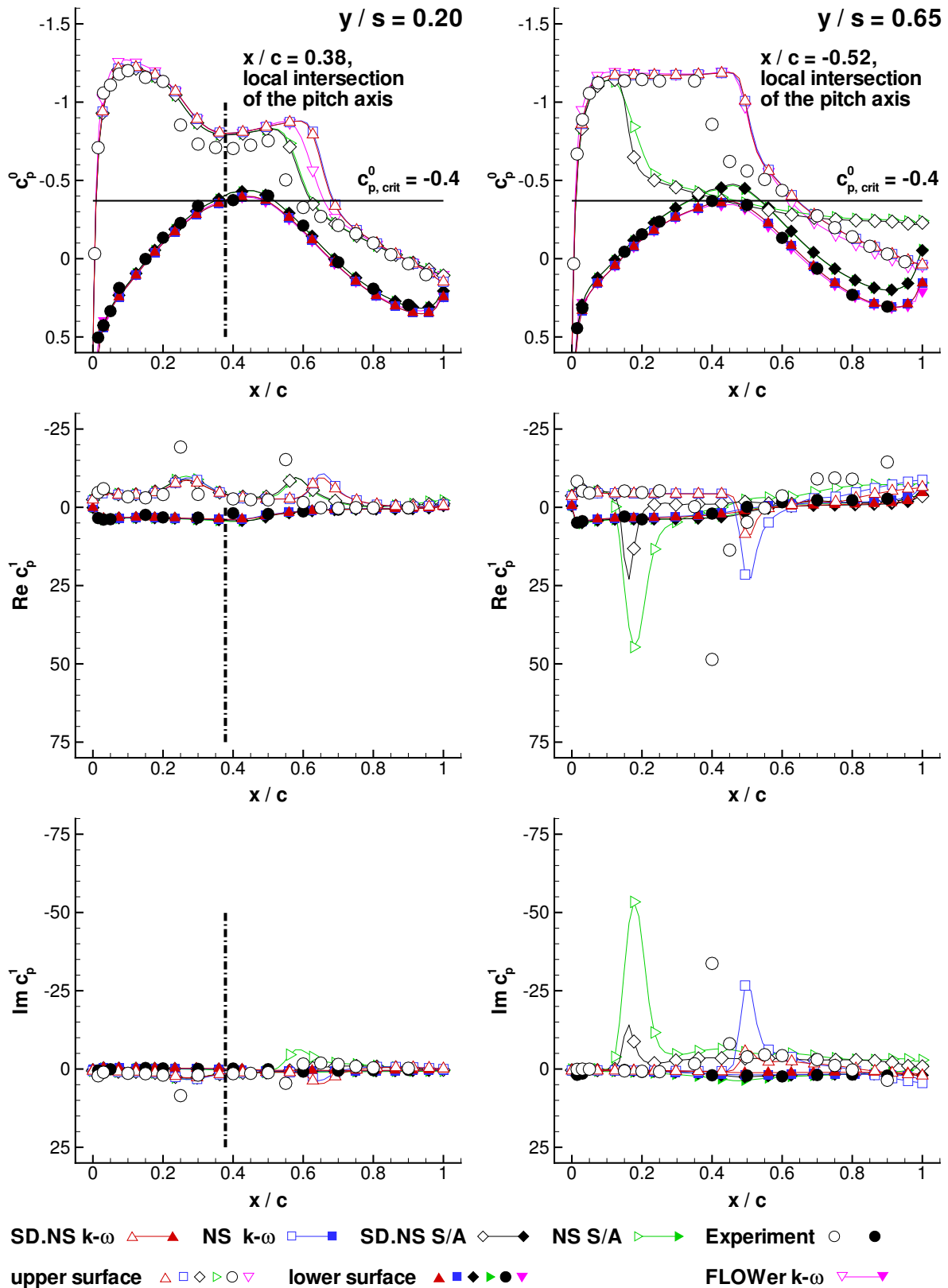
Fig. 10 Comparison of the zeroth- and first-harmonic pressure coefficient distributions (c_p^0 and c_p^1) for the LANNW case CT9 ($Ma_\infty = 0.82$, $Re_\infty = 7.2 \times 10^6$, $\breve{\alpha} = 2.60$ deg, $\breve{\alpha} = 0.25$ deg, $k_{red} = 0.560$, $x_p/c_r = 0.62$)

cients (Table 5), c_L^0 gained from FLM-SD.NS k-ω agrees excellently to its FLM-NS k-ω counterpart. Either c_L^0-prediction is again confirmed

FLM-method	c_L^0	$Re\,c_L^1$	$Im\,c_L^1$
SD.NS k-ω	0.636	5.208	-0.184
NS k-ω	0.638	4.798	0.614
SD.NS S/A	0.484	4.784	1.737
NS S/A	0.490	4.051	2.504

FLM-method	c_M^0	$Re\,c_M^1$	$Im\,c_M^1$
SD.NS k-ω	-0.229	-1.587	-0.421
NS k-ω	-0.230	-1.200	-1.083
SD.NS S/A	-0.133	-0.917	-2.000
NS S/A	-0.134	-0.451	-1.739

Table 5 Comparison of the global load coefficients for the LANNW case CT9 ($Ma_\infty = 0.82$, $Re_\infty = 7.2 \times 10^6$, $\check{\alpha} = 2.60$ deg, $\check{\alpha} = 0.25$ deg, $k_{red} = 0.560$, $x_p/c_r = 0.62$)

by FLOWer k-ω with a value of 0.626 – a deviation of merely 2%, just as seen for the CT5 case. Where conformity in the FLM-SD.NS-k-ω- and FLM-NS-k-ω-computed $Re\,c_L^1$ had been established for CT5, a spread of 9% between the two instances is now observed. This circumstance can be made attributable to the strongly differing magnitude prediction of the $Re\,c_p^1$-peak associated with the SSF-terminating shock at the localities of flow detachment. For the corresponding $Im\,c_p^1$-peak, the magnitude deviation between the two methods is even more pronounced, especially when taking into account the otherwise minute value of the upper-/lower-surface $Im\,c_p^1$ progressions. Similar to the CT2 case, both $Im\,c_L^1$-predictions are an order of magnitude smaller in absolute value than their $Re\,c_L^1$ counterparts. FLM-SD.NS-k-ω-computed $Im\,c_L^1$, however, exhibits a negative sign, while only having a third of the FLM-NS-k-ω-computed instance's absolute value: Integrating over the entire wing, the positive $\Delta Im\,c_p^1$ of the pertinent shock region, has compensated only partially for the otherwise negative one. Whereas FLM-

SD.NS-k-ω now indicates a time-dependent c_L that again marginally lags the excitation ($\check{\varphi}_{c_L^1} \approx -2$ deg), FLM-NS-k-ω renders one that minimally leads ($\check{\varphi}_{c_L^1} \approx 7$ deg). For either method, however, the time-dependent c_L may just as well be perceived as being entirely in phase. FLM-SD.NS-S/A-computed c_L^0 is 24% lower than its k-ω counterpart, a difference accrued through the substantially farther upstream prediction of the SSF-terminating shock ($\approx 23\%\,c$ at greatest) for the localities of flow detachment – thus yielding a significantly smaller sectional c_L^0 – across the semispan. In contrast, FLM-SD.NS-S/A-computed $Re\,c_L^1$ is merely 8% lower than its k-ω counterpart. Then again, the corresponding $Im\,c_L^1$ exhibits the greatest turbulence-model-induced variation of all three test cases, being an order of magnitude greater in absolute value than the FLM-SD.NS-k-ω-computed instance, while having a positive sign. Primarily, the changes seen in both $Re\,c_L^1$ and $Im\,c_L^1$ can be, respectively, made attributable to the k-ω-differing upper-surface $Re\,c_p^1$- and $Im\,c_p^1$-progression for the shock/post-shock region at localities of flow detachment. A singular aspect, such as the deviating prediction of the c_p^1-peak associated with the SSF-terminating shock, however, cannot be unambiguously picked out. Whereas FLM-SD.NS-S/A- and FLM-NS-S/A-computed c_L^0 are practically identical, the spreads for $Re\,c_L^1$ and $Im\,c_L^1$ are substantial: 18% and 31%, respectively. Still, FLM-SD.NS-S/A and FLM-NS-S/A conform in their indication of a time-dependent c_L that distinctly leads the excitation, contrary to the k-ω predictions. They strongly differ, however, in $\check{\varphi}_{c_L^1}$, respectively, being ≈ 20 deg and ≈ 32 deg.

FLM-SD.NS-k-ω-predicted c_M^0 is nearly identical to its FLM-NS k-ω counterpart. They are confirmed by the FLOWer k-ω-computed c_M^0 of -0.222 value – a deviation of merely 3%, just as seen for the CT5 case. Once again, where conformity in the FLM-SD.NS-k-ω- and FLM-NS k-ω-predicted $Re\,c_M^1$ had been established for CT5, a spread of 32% between the two instances is observed. Evidently, the circumstances already responsible for the difference in computed

$Re\,c_L^1$ are strongly amplified when leverage towards the pitch axis is accounted for. This is witnessed even more so in $Im\,c_M^1$, where in absolute value the FLM-SD.NS-k-ω-computed instance is only a third of its FLM-NS k-ω counterpart. In contrast to both CT2 and CT5, however, either $Im\,c_M^1$ emerges in the same order of magnitude as $Re\,c_M^1$, making such a deviation no longer tolerable. Even though FLM-SD.NS k-ω and FLM-NS k-ω conform in their indication of a time-dependent c_M that distinctly lags the excitation, they strongly differ in their prediction of $\check{\phi}_{c_M^1}$, respectively, ≈ -15 deg and ≈ -42 deg. In regard to a free pitching oscillation, FLM-SD.NS k-ω would thus render a substantially lesser measure of dynamic stability. In absolute value, FLM-SD.NS-S/A-predicted c_M^0 is now about half its k-ω counterpart, a behavior again consistent with the SSF-terminating shock's farther upstream prediction at the localities of flow detachment. A similar change can be witnessed for $Re\,c_M^1$, whereas FLM-SD.NS-S/A-predicted $Im\,c_M^1$ has five times the absolute value of its k-ω counterpart. Notably differing form CT2 and CT5, the absolute value of $Im\,c_M^1$ has become twice that of $Re\,c_M^1$. FLM-SD.NS- and FLM-NS-computed c_M^0 instances can again be considered equal for the S/A turbulence model. In regard to $Re\,c_M^1$, the spread between the two methods has substantially widened, with the FLM-SD.NS-S/A prediction having twice the absolute value of its FLM-NS-S/A counterpart. Contrarily, the 15% deviation exhibited by $Im\,c_M^1$ actually represents an improvement. In analogy to both CT2 and CT5, the greater sensitivity of $Im\,c_L^1$ to the choice of turbulence model has followed through to $Im\,c_M^1$. The same, however, can no longer be said with respect to the method type, as $Re\,c_L^1$ now sees its spread more strongly amplified towards $Re\,c_M^1$. Both FLM-SD.NS S/A and FLM-NS S/A render a time-dependent c_M that lags the excitation by somewhat more than a quarter cycle: Despite the deviations, they conform surprisingly well in their predicted $\check{\phi}_{c_M^1}$ instances, respectively, being ≈ -115 and ≈ -104 deg. In regard to the free pitching oscillation, the S/A

turbulence model would thus indicate a substantially higher degree of dynamic stability than its k-ω counterpart.

Overall, FLM-SD.NS k-ω renders the unsteady loading of the spanwise-λ-shock/detached-flow case in less than satisfactory agreement to FLM-NS k-ω. The same can be said for FLM-SD.NS S/A with respect to FLM-NS S/A. For this particular test case, however, a substantial degree of nonlinear interaction is known to physically exist: Despite an improved prediction of the time-invariant mean flowfield through the Wilcox k-ω turbulence model, the limitations inherent to the small disturbance approach are still predominant.

6 Computational Efficiency

As documented in Table 6 and Table 7, FLM-SD.NS retains the established computational efficiency gain over its FLM-NS counterpart even in their k-ω incarnations, reducing computation times by up to an half order of magnitude for the investigated cases. With the exception of

Case	$\check{t}_{CPU}^{SD.NS}\|_{k-\omega}$, h	$\check{t}_{CPU}^{NS}\|_{k-\omega}$, h	ζ_{CPU}
CT2	84.8	190.4	2.2
CT5	30.0	120.5	4.0
CT9	30.2	90.8	3.0

Table 6 Comparison of computational effort between FLM-SD.NS k-ω and FLM-NS k-ω for the LANNW cases

Case	$\check{t}_{CPU}^{SD.NS}\|$S/A, h	$\check{t}_{CPU}^{NS}\|$S/A, h	ζ_{CPU}
CT2	33.9	99.1	2.9
CT5	24.1	88.0	3.7
CT9	173.5	312.0[a]	1.8

[a] 12 oscillation cycles computed

Table 7 Comparison of computational effort between FLM-SD.NS S/A and FLM-NS S/A for the LANNW cases

CT9, however, FLM-SD.NS/FLM-NS k-ω com-

putation times are substantially higher than those of FLM-SD.NS/FLM-NS S/A. In this regard, Table 8 reveals that the bare computational effort of FLM-SD.NS k-ω is 55% higher than that of FLM-SD.NS S/A, while allocating 27% more memory. Contrarily, the bare computational effort of FLM-NS k-ω is 20% higher than that of FLM-NS S/A, while allocating merely 10% more memory. Thus, the penalties already inherent to the dynamically fully nonlinear k-ω implementation become amplified towards the small disturbance one. Nevertheless, as FLM-SD.NS k-ω scales to FLM-NS k-ω in both computational effort and memory requirements nearly the same way FLM-SD.NS S/A does to FLM-NS S/A, no significant relative penalty can be said to have occurred.

FLM-method	$\bar{t}_{CPU}^{method\,a}$, μs	RAM^a, KB
SD.NS k-ω	76	6.2
NS k-ω	12	1.2
SD.NS S/A	49	4.9
NS S/A	10	1.1

^{a} per pseudotime step and per cell

Table 8 Comparison of the test-case-averaged computational effort, discounting the convergence rate, and memory requirements for all FLM-methods

7   Conclusions

In an effort to extend FLM-SD.NS's range of applicability, a dynamically linear instance of the Wilcox k-ω turbulence model as incorporated into the small disturbance Navier-Stokes equations has been implemented. FLM-SD.NS k-ω computational results for LANNW harmonic pitching oscillations were presented and compared with those of FLM-NS k-ω, FLM-SD.NS/FLM-NS S/A, as well as experimental data, and a FLOWer k-ω steady result. For the attached-flow cases, FLM-SD.NS k-ω yields equally accurate predictions as FLM-SD.NS S/A. Reductions in computation time, up to half an order of magnitude, in relation to FLM-NS k-ω

are ascertained. Naturally, absolute computation times of FLM-SD.NS k-ω are higher than those of FLM-SD.NS S/A. For the detached-flow case, the primary benefit of the Wilcox k-ω turbulence model lies in an FLM-NS-supplied time-invariant mean flowfield that better represents the actual physical one. Consequently, in production cases where the flowfield's development is not a priori known, FLM-SD.NS k-ω can offer an advantage over FLM-SD.NS S/A. Prediction accuracy, however, will be increasingly compromised the more extensive any underlyingly-rendered flow detachment becomes.

8   Acknowledgments

References

[1] Dufour, G., Sicot, F., Puigt, G., Liauzun, C., and Dugeai, A. Contrasting the harmonic balance and linearized methods for oscillating-flap simulations. *AIAA Journal*, Vol. 48, No 4, pp 788–797, 2010.

[2] Holmes, D. G., Mitchell, B. E., and Lorence, C. B. Three dimensional linearized Navier-Stokes calculations for flutter and forced response. *Proc 8th International Symposium on Unsteady Aerodynamics and Aeroelasticity of Turbomachines held in Stockholm, Sweden, 14th-18th Sept. 1997*, pp 211–224, Dordrecht, Netherlands, 1998. Kluwer Academic Publishers.

[3] Iatrou, M. Ein Navier-Stokes-Verfahren kleiner Störungen für instationäre Vorgänge - Anwendung auf Transportflugzeuge. Ph.D. Dissertation, Institute of Aerodynamics, Technische Universität München, Garching, Germany, Nov. 2009.

[4] Kroll, N., Rossow, C. C., Schwamborn, D., Becker, K., and Heller, G. MEGAFLOW - A numerical flow simulation tool for transport aircraft design. 23rd Congress of the International

Council of the Aeronautical Sciences, ICAS Paper 2002-1.10.5, Toronto, CA, Sep. 2002.

[5] Liauzun, C., Canonne, E., and Mortchéléwicz, G. D. Flutter numerical computations using the linearized Navier-Stokes equations. *Proc Advanced Methods in Aeroelasticity*, pp 8–1–8–12, RTO-MP-AVT-154, Loen, Norway, May 2008.

[6] Menter, F. R. Two-equation eddy-viscosity turbulence models for engineering applications. *AIAA Journal*, Vol. 32, No 8, pp 1598–1605, 1994.

[7] Pechloff, A. and Laschka, B. Small disturbance Navier-Stokes method: Efficient tool for predicting unsteady air loads. *Journal of Aircraft*, Vol. 43, No 1, pp 17–29, 2006.

[8] Pechloff, A. and Laschka, B. Small disturbance Navier-Stokes computations for low-aspect-ratio-wing pitching oscillations. *Journal of Aircraft*, Vol. 47, No 3, pp 737–753, 2010.

[9] Rung, T. and Thiele, F. Computational modelling of complex boundary-layer flows. *Proc 9th International Symposium on Transport Phenomena in Thermal-Fluid Engineering*, pp 321–326, Singapore, 1996.

[10] Schuster, D. M., Liu, D. D., and Huttsell, L. J. Computational aeroelasticity: Success, progress, challenge. *Journal of Aircraft*, Vol. 40, No 5, pp 843–856, 2003.

[11] Spalart, P. R., and Allmaras, S. R. A one-equation turbulence model for aerodynamic flows. AIAA Paper 92-0439, Jan. 1992.

[12] Wilcox, D. C. Reassessment of the scale-determining equation for advanced turbulence models. *AIAA Journal*, Vol. 26, No 11, pp 1299–1310, 1988.

[13] Zwaan, R. J. LANN Wing pitching oscillation. Compendium of Unsteady Aerodynamic Measurements, Addendum No. 1, AGARD-R-702, 1985, pp. 9-1–9-76.

A Supplemental Relations

- Amplitude and time-invariant mean thermal equation of state:

$$\hat{T} = (\hat{p} - \hat{\rho}\,\bar{T})/\bar{\rho}, \qquad \bar{T} = \bar{p}/\bar{\rho}. \qquad (21)$$

- Amplitude and time-invariant mean static pressure:

$$
\hat{p} = \Gamma\left(\widehat{\rho e} + \hat{\rho}\,\frac{\overline{\rho u^2} + \overline{\rho v^2} + \overline{\rho w^2}}{2\bar{\rho}^2} \right.
$$
$$
- \frac{\overline{\rho u}\,\widehat{\rho u} + \overline{\rho v}\,\widehat{\rho v} + \overline{\rho w}\,\widehat{\rho w}}{\bar{\rho}}
$$
$$
\left. - \widehat{\rho k} \right),
$$
$$
\bar{p} = \Gamma\left(\overline{\rho e} - \frac{\overline{\rho u^2} + \overline{\rho v^2} + \overline{\rho w^2}}{2\bar{\rho}^2} - \overline{\rho k} \right).
$$
$$(22)$$

- Amplitude and time-invariant mean molecular viscosity:

$$
\hat{\mu} = \frac{\bar{\mu}}{\bar{T}+S}\left[\frac{3(\bar{T}+S)}{2\bar{T}} - 1\right]\hat{T},
$$
$$
\bar{\mu} = \bar{\mu}_\infty\,\bar{T}^{\frac{3}{2}}\,\frac{1+S}{\bar{T}+S}.
$$
$$(23)$$

- Diagonal components of the amplitude laminar shear-stress tensor:

$$
\hat{\tau}_{xx,l} = \frac{2}{3}\bar{\mu}\left(2\frac{\partial\hat{u}}{\partial x} - \frac{\partial\hat{v}}{\partial y} - \frac{\partial\hat{w}}{\partial z}\right)
$$
$$
+ \frac{2}{3}\hat{\mu}\left(2\frac{\partial\bar{u}}{\partial x} - \frac{\partial\bar{v}}{\partial y} - \frac{\partial\bar{w}}{\partial z}\right),
$$
$$
\hat{\tau}_{yy,l} = \frac{2}{3}\bar{\mu}\left(2\frac{\partial\hat{v}}{\partial y} - \frac{\partial\hat{u}}{\partial x} - \frac{\partial\hat{w}}{\partial z}\right)
$$
$$
+ \frac{2}{3}\hat{\mu}\left(2\frac{\partial\bar{v}}{\partial y} - \frac{\partial\bar{u}}{\partial x} - \frac{\partial\bar{w}}{\partial z}\right),
$$
$$
\hat{\tau}_{zz,l} = \frac{2}{3}\bar{\mu}\left(2\frac{\partial\hat{w}}{\partial z} - \frac{\partial\hat{u}}{\partial x} - \frac{\partial\hat{v}}{\partial y}\right)
$$
$$
+ \frac{2}{3}\hat{\mu}\left(2\frac{\partial\bar{w}}{\partial z} - \frac{\partial\bar{u}}{\partial x} - \frac{\partial\bar{v}}{\partial y}\right).
$$
$$(24)$$

- Off-diagonal components of the amplitude laminar shear-stress tensor:

$$
\begin{aligned}
\hat{\tau}_{xy,l} = \hat{\tau}_{yx,l} &= \bar{\mu}\left(\frac{\partial \hat{u}}{\partial y} + \frac{\partial \hat{v}}{\partial x}\right) \\
&+ \hat{\mu}\left(\frac{\partial \bar{u}}{\partial y} + \frac{\partial \bar{v}}{\partial x}\right), \\
\hat{\tau}_{xz,l} = \hat{\tau}_{zx,l} &= \bar{\mu}\left(\frac{\partial \hat{u}}{\partial z} + \frac{\partial \hat{w}}{\partial x}\right) \\
&+ \hat{\mu}\left(\frac{\partial \bar{u}}{\partial z} + \frac{\partial \bar{w}}{\partial x}\right), \\
\hat{\tau}_{yz,l} = \hat{\tau}_{zy,l} &= \bar{\mu}\left(\frac{\partial \hat{v}}{\partial z} + \frac{\partial \hat{w}}{\partial y}\right) \\
&+ \hat{\mu}\left(\frac{\partial \bar{v}}{\partial z} + \frac{\partial \bar{w}}{\partial y}\right).
\end{aligned}
\tag{25}
$$

- Diagonal components of the time-invariant mean laminar shear-stress tensor:

$$
\begin{aligned}
\bar{\tau}_{xx,l} &= \frac{2}{3}\bar{\mu}\left(2\frac{\partial \bar{u}}{\partial x} - \frac{\partial \bar{v}}{\partial y} - \frac{\partial \bar{w}}{\partial z}\right), \\
\bar{\tau}_{yy,l} &= \frac{2}{3}\bar{\mu}\left(2\frac{\partial \bar{v}}{\partial y} - \frac{\partial \bar{u}}{\partial x} - \frac{\partial \bar{w}}{\partial z}\right), \\
\bar{\tau}_{zz,l} &= \frac{2}{3}\bar{\mu}\left(2\frac{\partial \bar{w}}{\partial z} - \frac{\partial \bar{u}}{\partial x} - \frac{\partial \bar{v}}{\partial y}\right).
\end{aligned}
\tag{26}
$$

- Off-diagonal components of the time-invariant mean laminar shear-stress tensor:

$$
\begin{aligned}
\bar{\tau}_{xy} = \bar{\tau}_{yx} &= \bar{\mu}\left(\frac{\partial \bar{u}}{\partial y} + \frac{\partial \bar{v}}{\partial x}\right), \\
\bar{\tau}_{xz} = \bar{\tau}_{zx} &= \bar{\mu}\left(\frac{\partial \bar{u}}{\partial z} + \frac{\partial \bar{w}}{\partial x}\right), \\
\bar{\tau}_{yz} = \bar{\tau}_{zy} &= \bar{\mu}\left(\frac{\partial \bar{v}}{\partial z} + \frac{\partial \bar{w}}{\partial y}\right).
\end{aligned}
\tag{27}
$$

- Diagonal components of the amplitude turbulent shear-stress tensor:

$$
\begin{aligned}
\hat{\tau}_{xx,t} &= \frac{2}{3}\bar{\mu}_t\left(2\frac{\partial \hat{u}}{\partial x} - \frac{\partial \hat{v}}{\partial y} - \frac{\partial \hat{w}}{\partial z}\right) \\
&+ \frac{2}{3}\hat{\mu}_t\left(2\frac{\partial \bar{u}}{\partial x} - \frac{\partial \bar{v}}{\partial y} - \frac{\partial \bar{w}}{\partial z}\right) - \frac{2}{3}\widehat{\rho k}, \\
\hat{\tau}_{yy,t} &= \frac{2}{3}\bar{\mu}_t\left(2\frac{\partial \hat{v}}{\partial y} - \frac{\partial \hat{u}}{\partial x} - \frac{\partial \hat{w}}{\partial z}\right) \\
&+ \frac{2}{3}\hat{\mu}_t\left(2\frac{\partial \bar{v}}{\partial y} - \frac{\partial \bar{u}}{\partial x} - \frac{\partial \bar{w}}{\partial z}\right) - \frac{2}{3}\widehat{\rho k}, \\
\hat{\tau}_{zz,t} &= \frac{2}{3}\bar{\mu}_t\left(2\frac{\partial \hat{w}}{\partial z} - \frac{\partial \hat{u}}{\partial x} - \frac{\partial \hat{v}}{\partial y}\right) \\
&+ \frac{2}{3}\hat{\mu}_t\left(2\frac{\partial \bar{w}}{\partial z} - \frac{\partial \bar{u}}{\partial x} - \frac{\partial \bar{v}}{\partial y}\right) - \frac{2}{3}\widehat{\rho k}.
\end{aligned}
\tag{28}
$$

- Off-diagonal components of the amplitude turbulent shear-stress tensor:

$$
\begin{aligned}
\hat{\tau}_{xy,t} = \hat{\tau}_{yx,t} &= \bar{\mu}_t\left(\frac{\partial \hat{u}}{\partial y} + \frac{\partial \hat{v}}{\partial x}\right) \\
&+ \hat{\mu}_t\left(\frac{\partial \bar{u}}{\partial y} + \frac{\partial \bar{v}}{\partial x}\right), \\
\hat{\tau}_{xz,t} = \hat{\tau}_{zx,t} &= \bar{\mu}_t\left(\frac{\partial \hat{u}}{\partial z} + \frac{\partial \hat{w}}{\partial x}\right) \\
&+ \hat{\mu}_t\left(\frac{\partial \bar{u}}{\partial z} + \frac{\partial \bar{w}}{\partial x}\right), \\
\hat{\tau}_{yz,t} = \hat{\tau}_{zy,t} &= \bar{\mu}_t\left(\frac{\partial \hat{v}}{\partial z} + \frac{\partial \hat{w}}{\partial y}\right) \\
&+ \hat{\mu}_t\left(\frac{\partial \bar{v}}{\partial z} + \frac{\partial \bar{w}}{\partial y}\right).
\end{aligned}
\tag{29}
$$

- Diagonal components of the time-invariant mean turbulent shear-stress tensor:

$$
\begin{aligned}
\bar{\tau}_{xx,t} &= \frac{2}{3}\bar{\mu}_t\left(2\frac{\partial \bar{u}}{\partial x} - \frac{\partial \bar{v}}{\partial y} - \frac{\partial \bar{w}}{\partial z}\right) - \frac{2}{3}\overline{\rho k}, \\
\bar{\tau}_{yy,t} &= \frac{2}{3}\bar{\mu}_t\left(2\frac{\partial \bar{v}}{\partial y} - \frac{\partial \bar{u}}{\partial x} - \frac{\partial \bar{w}}{\partial z}\right) - \frac{2}{3}\overline{\rho k}, \\
\bar{\tau}_{zz,t} &= \frac{2}{3}\bar{\mu}_t\left(2\frac{\partial \bar{w}}{\partial z} - \frac{\partial \bar{u}}{\partial x} - \frac{\partial \bar{v}}{\partial y}\right) - \frac{2}{3}\overline{\rho k}.
\end{aligned}
\tag{30}
$$

- Off-diagonal components of the time-invariant mean turbulent shear-stress tensor:

$$\bar{\tau}_{xy,t} = \bar{\tau}_{yx,t} = \bar{\mu}_t \left(\frac{\partial \bar{u}}{\partial y} + \frac{\partial \bar{v}}{\partial x} \right),$$

$$\bar{\tau}_{xz,t} = \bar{\tau}_{zx,t} = \bar{\mu}_t \left(\frac{\partial \bar{u}}{\partial z} + \frac{\partial \bar{w}}{\partial x} \right), \quad (31)$$

$$\bar{\tau}_{yz,t} = \bar{\tau}_{zy,t} = \bar{\mu}_t \left(\frac{\partial \bar{v}}{\partial z} + \frac{\partial \bar{w}}{\partial y} \right).$$

- Components of the amplitude total shear-stress tensor:

$$\hat{\tau}_{xx} = \hat{\tau}_{xx,l} + \hat{\tau}_{xx,t}, \quad \hat{\tau}_{xy} = \hat{\tau}_{yx} = \hat{\tau}_{yx,l} + \hat{\tau}_{yx,t},$$

$$\hat{\tau}_{yy} = \hat{\tau}_{yy,l} + \hat{\tau}_{yy,t}, \quad \hat{\tau}_{xz} = \hat{\tau}_{zx} = \hat{\tau}_{zx,l} + \hat{\tau}_{zx,t},$$

$$\hat{\tau}_{zz} = \hat{\tau}_{zz,l} + \hat{\tau}_{zz,t}, \quad \hat{\tau}_{yz} = \hat{\tau}_{zy} = \hat{\tau}_{zy,l} + \hat{\tau}_{zy,t}.$$

$$(32)$$

- Components of the time-invariant mean total shear-stress tensor:

$$\bar{\tau}_{xx} = \bar{\tau}_{xx,l} + \bar{\tau}_{xx,t}, \quad \bar{\tau}_{xy} = \bar{\tau}_{yx} = \bar{\tau}_{yx,l} + \bar{\tau}_{yx,t},$$

$$\bar{\tau}_{yy} = \bar{\tau}_{yy,l} + \bar{\tau}_{yy,t}, \quad \bar{\tau}_{xz} = \bar{\tau}_{zx} = \bar{\tau}_{zx,l} + \bar{\tau}_{zx,t},$$

$$\bar{\tau}_{zz} = \bar{\tau}_{zz,l} + \bar{\tau}_{zz,t}, \quad \bar{\tau}_{yz} = \bar{\tau}_{zy} = \bar{\tau}_{zy,l} + \bar{\tau}_{zy,t}.$$

$$(33)$$

- Amplitude Cartesian energy-flux:

$$
\begin{aligned}
\hat{\Pi}_x &= \bar{u}\hat{\tau}_{xx} + \bar{v}\hat{\tau}_{xy} + \bar{w}\hat{\tau}_{xz} \\
&+ \hat{u}\bar{\tau}_{xx} + \hat{v}\bar{\tau}_{xy} + \hat{w}\bar{\tau}_{xz} + \hat{\tau}_{kx} - \hat{q}_x,
\end{aligned}
$$

$$
\begin{aligned}
\hat{\Pi}_y &= \bar{u}\hat{\tau}_{yx} + \bar{v}\hat{\tau}_{yy} + \bar{w}\hat{\tau}_{yz} \\
&+ \hat{u}\bar{\tau}_{yx} + \hat{v}\bar{\tau}_{yy} + \hat{w}\bar{\tau}_{yz} + \hat{\tau}_{ky} - \hat{q}_y,
\end{aligned}
$$

$$
\begin{aligned}
\hat{\Pi}_z &= \bar{u}\hat{\tau}_{zx} + \bar{v}\hat{\tau}_{zy} + \bar{w}\hat{\tau}_{zz} \\
&+ \hat{u}\bar{\tau}_{zx} + \hat{v}\bar{\tau}_{zy} + \hat{w}\bar{\tau}_{zz} + \hat{\tau}_{kz} - \hat{q}_z.
\end{aligned}
$$

$$(34)$$

- Time-invariant mean Cartesian energy-flux:

$$\bar{\Pi}_x = \bar{u}\bar{\tau}_{xx} + \bar{v}\bar{\tau}_{xy} + \bar{w}\bar{\tau}_{xz} + \bar{\tau}_{kx} - \bar{q}_x,$$

$$\bar{\Pi}_y = \bar{u}\bar{\tau}_{yx} + \bar{v}\bar{\tau}_{yy} + \bar{w}\bar{\tau}_{yz} + \bar{\tau}_{ky} - \bar{q}_y,$$

$$\bar{\Pi}_z = \bar{u}\bar{\tau}_{zx} + \bar{v}\bar{\tau}_{zy} + \bar{w}\bar{\tau}_{zz} + \bar{\tau}_{kz} - \bar{q}_z.$$

$$(35)$$

- Components of the amplitude Cartesian heat-flux vector:

$$
\begin{aligned}
\hat{q}_x &= -\frac{\gamma}{\Gamma} \left[\left(\frac{\bar{\mu}}{Pr} + \frac{\bar{\mu}_t}{Pr_t} \right) \frac{\partial \hat{T}}{\partial x} \right. \\
&\left. + \left(\frac{\hat{\mu}}{Pr} + \frac{\hat{\mu}_t}{Pr_t} \right) \frac{\partial \bar{T}}{\partial x} \right],
\end{aligned}
$$

$$
\begin{aligned}
\hat{q}_y &= -\frac{\gamma}{\Gamma} \left[\left(\frac{\bar{\mu}}{Pr} + \frac{\bar{\mu}_t}{Pr_t} \right) \frac{\partial \hat{T}}{\partial y} \right. \\
&\left. + \left(\frac{\hat{\mu}}{Pr} + \frac{\hat{\mu}_t}{Pr_t} \right) \frac{\partial \bar{T}}{\partial y} \right],
\end{aligned}
$$

$$
\begin{aligned}
\hat{q}_z &= -\frac{\gamma}{\Gamma} \left[\left(\frac{\bar{\mu}}{Pr} + \frac{\bar{\mu}_t}{Pr_t} \right) \frac{\partial \hat{T}}{\partial z} \right. \\
&\left. + \left(\frac{\hat{\mu}}{Pr} + \frac{\hat{\mu}_t}{Pr_t} \right) \frac{\partial \bar{T}}{\partial z} \right].
\end{aligned}
$$

$$(36)$$

- Components of the time-invariant mean Cartesian heat-flux vector:

$$\bar{q}_x = -\frac{\gamma}{\Gamma} \left[\left(\frac{\bar{\mu}}{Pr} + \frac{\bar{\mu}_t}{Pr_t} \right) \frac{\partial \bar{T}}{\partial x} \right],$$

$$\bar{q}_y = -\frac{\gamma}{\Gamma} \left[\left(\frac{\bar{\mu}}{Pr} + \frac{\bar{\mu}_t}{Pr_t} \right) \frac{\partial \bar{T}}{\partial y} \right], \quad (37)$$

$$\bar{q}_z = -\frac{\gamma}{\Gamma} \left[\left(\frac{\bar{\mu}}{Pr} + \frac{\bar{\mu}_t}{Pr_t} \right) \frac{\partial \bar{T}}{\partial z} \right].$$

- Amplitude shear-stress-equivalent k-terms:

$$\hat{\tau}_{kx} = (\hat{\mu} + \sigma_k \hat{\mu}_t) \frac{\partial \bar{k}}{\partial x} + (\bar{\mu} + \sigma_k \bar{\mu}_t) \frac{\partial \hat{k}}{\partial x},$$

$$\hat{\tau}_{ky} = (\hat{\mu} + \sigma_k \hat{\mu}_t) \frac{\partial \bar{k}}{\partial y} + (\bar{\mu} + \sigma_k \bar{\mu}_t) \frac{\partial \hat{k}}{\partial y},$$

$$\hat{\tau}_{kz} = (\hat{\mu} + \sigma_k \hat{\mu}_t) \frac{\partial \bar{k}}{\partial z} + (\bar{\mu} + \sigma_k \bar{\mu}_t) \frac{\partial \hat{k}}{\partial z}.$$

$$(38)$$

- Amplitude shear-stress-equivalent ω-terms:

$$\hat{\tau}_{\omega x} = (\hat{\mu} + \sigma_\omega \hat{\mu}_t)\frac{\partial\bar{\omega}}{\partial x} + (\bar{\mu} + \sigma_\omega \bar{\mu}_t)\frac{\partial\hat{\omega}}{\partial x},$$

$$\hat{\tau}_{\omega y} = (\hat{\mu} + \sigma_\omega \hat{\mu}_t)\frac{\partial\bar{\omega}}{\partial y} + (\bar{\mu} + \sigma_\omega \bar{\mu}_t)\frac{\partial\hat{\omega}}{\partial y},$$

$$\hat{\tau}_{\omega z} = (\hat{\mu} + \sigma_\omega \hat{\mu}_t)\frac{\partial\bar{\omega}}{\partial z} + (\bar{\mu} + \sigma_\omega \bar{\mu}_t)\frac{\partial\hat{\omega}}{\partial z}.$$

$$(39)$$

- Time-invariant mean shear-stress-equivalent k-, ω-terms:

$$\bar{\tau}_{kx} = (\bar{\mu} + \sigma_k\bar{\mu}_t)\frac{\partial\bar{k}}{\partial x}, \quad \bar{\tau}_{\omega x} = (\bar{\mu} + \sigma_\omega\bar{\mu}_t)\frac{\partial\bar{\omega}}{\partial x},$$

$$\bar{\tau}_{ky} = (\bar{\mu} + \sigma_k\bar{\mu}_t)\frac{\partial\bar{k}}{\partial y}, \quad \bar{\tau}_{\omega x} = (\bar{\mu} + \sigma_\omega\bar{\mu}_t)\frac{\partial\bar{\omega}}{\partial y},$$

$$\bar{\tau}_{kz} = (\bar{\mu} + \sigma_k\bar{\mu}_t)\frac{\partial\bar{k}}{\partial z}, \quad \bar{\tau}_{\omega x} = (\bar{\mu} + \sigma_\omega\bar{\mu}_t)\frac{\partial\bar{\omega}}{\partial z}.$$

$$(40)$$

- Amplitude k-production:

$$\begin{aligned}\hat{P}_k =\ & \bar{\tau}_{xx,t}\frac{\partial\hat{u}}{\partial x} + \bar{\tau}_{xy,t}\left(\frac{\partial\hat{u}}{\partial y} + \frac{\partial\hat{v}}{\partial x}\right) \\ & + \bar{\tau}_{yy,t}\frac{\partial\hat{v}}{\partial y} + \bar{\tau}_{yz,t}\left(\frac{\partial\hat{v}}{\partial z} + \frac{\partial\hat{w}}{\partial y}\right) \\ & + \bar{\tau}_{zz,t}\frac{\partial\hat{w}}{\partial z} + \bar{\tau}_{zx,t}\left(\frac{\partial\hat{u}}{\partial z} + \frac{\partial\hat{w}}{\partial x}\right) \\ & + \hat{\tau}_{xx,t}\frac{\partial\bar{u}}{\partial x} + \hat{\tau}_{xy,t}\left(\frac{\partial\bar{u}}{\partial y} + \frac{\partial\bar{v}}{\partial x}\right) \\ & + \hat{\tau}_{yy,t}\frac{\partial\bar{v}}{\partial y} + \hat{\tau}_{yz,t}\left(\frac{\partial\bar{v}}{\partial z} + \frac{\partial\bar{w}}{\partial y}\right) \\ & + \hat{\tau}_{zz,t}\frac{\partial\bar{w}}{\partial z} + \hat{\tau}_{zx,t}\left(\frac{\partial\bar{u}}{\partial z} + \frac{\partial\bar{w}}{\partial x}\right).\end{aligned}$$

$$(41)$$

- Time-invariant mean k-production:

$$\begin{aligned}\bar{P}_k =\ & \bar{\tau}_{xx,t}\frac{\partial\bar{u}}{\partial x} + \bar{\tau}_{xy,t}\left(\frac{\partial\bar{u}}{\partial y} + \frac{\partial v}{\partial x}\right) \\ & + \bar{\tau}_{yy,t}\frac{\partial\bar{v}}{\partial y} + \bar{\tau}_{yz,t}\left(\frac{\partial\bar{v}}{\partial z} + \frac{\partial\bar{w}}{\partial y}\right) \\ & + \bar{\tau}_{zz,t}\frac{\partial\bar{w}}{\partial z} + \bar{\tau}_{zx,t}\left(\frac{\partial\bar{u}}{\partial z} + \frac{\partial\bar{w}}{\partial x}\right).\end{aligned}$$

$$(42)$$

- Amplitude and time-invariant mean k-destruction:

$$\hat{D}_k = \bar{D}_k\left(\frac{\hat{\rho}}{\bar{\rho}} + \frac{\hat{\omega}}{\bar{\omega}} + \frac{\hat{k}}{\bar{k}}\right), \quad \bar{D}_k = -c_{D_k}\bar{\rho}\bar{\omega}\bar{k}.$$

$$(43)$$

- Amplitude and time-invariant mean ω-production:

$$\hat{P}_\omega = \bar{P}_\omega\left(\frac{\hat{\omega}}{\bar{\omega}} - \frac{\hat{k}}{\bar{k}} + \frac{\hat{P}_k}{\bar{P}_k}\right), \quad \bar{P}_\omega = c_{P_\omega}\frac{\bar{\omega}}{\bar{k}}\bar{P}_k.$$

$$(44)$$

- Amplitude and time-invariant mean ω-destruction:

$$\hat{D}_\omega = \bar{D}_\omega\left(\frac{\hat{\rho}}{\bar{\rho}} + 2\frac{\hat{\omega}}{\bar{\omega}}\right), \quad \bar{D}_\omega = -c_{D_\omega}\bar{\rho}\bar{\omega}^2.$$

$$(45)$$

- Calibration coefficients:

$$\begin{aligned}\sigma_k &= 0.50, \quad \sigma_\omega = 0.50, \ \kappa = 0.41, \\ c_{P_k} &= 1.00, \quad c_{D_k} = 0.09, \\ c_{P_\omega} &= 0.56, \quad c_{D_\omega} = c_{D_k}\left(c_{P_\omega} + \frac{\sigma_\omega\kappa^2}{\sqrt{c_{D_k}}}\right).\end{aligned}$$

$$(46)$$